

Studying Light-Harvesting Models with Superconducting Circuits

Anton Potočník,^{1,*} Arno Bargerbos,^{1,*} Florian A. Y. N. Schröder,² Saeed A. Khan,³
 Michele C. Collodo,¹ Simone Gasparinetti,¹ Yves Salathé,¹ Celestino Creatore,²
 Christopher Eichler,¹ Hakan E. Türeci,³ Alex W. Chin,² and Andreas Wallraff¹

¹*Department of Physics, ETH Zürich, CH-8093, Zürich, Switzerland.*

²*Cavendish Laboratory, University of Cambridge,*

J. J. Thomson Avenue, Cambridge CB3 0HE, United Kingdom.

³*Department of Electrical Engineering, Princeton University, Princeton, New Jersey 08544, USA.*

The process of photosynthesis, the main source of energy in the animate world, converts sunlight into chemical energy. The surprisingly high efficiency of this process is believed to be enabled by an intricate interplay between the quantum nature of molecular structures in photosynthetic complexes and their interaction with the environment. Investigating these effects in biological samples is challenging due to their complex and disordered structure. Here we experimentally demonstrate a new approach for studying photosynthetic models based on superconducting quantum circuits. In particular, we demonstrate the unprecedented versatility and control of our method in an engineered three-site model of a pigment protein complex with realistic parameters scaled down in energy by a factor of 10^5 . With this system we show that the excitation transport between quantum coherent sites disordered in energy can be enabled through the interaction with environmental noise. We also show that the efficiency of the process is maximized for structured noise resembling intramolecular phononic environments found in photosynthetic complexes.

It is well accepted that the microscopic properties of all matter being composed of atoms and molecules are governed by the laws of quantum physics. At macroscopic scales, however, coherent quantum phenomena are frequently suppressed by the interaction with the environment. An intensely studied open question is, whether quantum mechanics plays an important functional role in biological processes. Examples of such processes are magneto reception in birds, olfaction and light harvesting, all studied in a field referred to as quantum biology¹⁻³. In particular, quantum coherent effects were observed in photosynthetic complexes by 2D electron spectroscopy at near ambient conditions⁴⁻⁶, which stimulated both experimental and theoretical work on light harvesting.

In a photosynthetic process light is captured in a molecular complex acting as an antenna. The created excitation is then relayed towards a reaction center through a network of chlorophyll molecules forming pigment protein complexes, such as the well studied Fenna-Matthews-Olson (FMO) complex^{1,2}. At the reaction center the excitation enables the synthesis of energy-rich molecules, e.g. adenosine triphosphate (ATP), relevant for supplying chemical energy throughout an organism. An excitation of an individual chlorophyll molecule is carried by a single chromophore whose highest occupied and lowest unoccupied molecular orbital can be approximated as a two-level system. The chlorophyll molecules form the sites of a network through which the individual excitations are transported. The energy levels of the individual sites and the coupling between the sites are affected by both static and dynamic disorder, which in uniform systems suppresses energy transfer between sites.

High efficiency energy transport between disordered sites is suggested to be enabled through the interaction

of the individual sites with vibrational modes of the protein scaffold into which the chlorophylls are embedded. A number of theoretical models have been developed to put this mechanism of efficient energy transport onto a solid footing⁷⁻¹¹. In particular it has been suggested that interactions between the energy levels of the chlorophyll molecules and the highly-structured phononic environment of the protein scaffold enhance directed excitation transport¹²⁻¹⁵.

The direct verification of these models is challenging due to the intricate structure and the limited control obtainable over photosynthetic complexes. Despite a number of theoretical studies, noise assisted energy transport (NAT) in biological systems has so far only been phenomenologically investigated on simple model systems with limited control over its parameters. Energy transport between two molecules placed on a substrate was studied with scanning tunneling microscopy¹⁶, using classical optics disorder was shown to break destructive interference and increase optical transmission¹⁷⁻¹⁹, similarly, disorder in the coupling parameter was shown to increase energy flow using classical electronic circuits²⁰ and in genetically engineered molecular systems energy transport was controlled by adjusting inter-chromophoric distances^{21,22}. Recently, a programmable nanophotonic processor was used to study transport properties in disordered systems²³.

In this work we demonstrate the use of superconducting quantum circuits^{24,25} to test models describing important aspects of photosynthesis, such as photon absorption and noise assisted excitation transport, with unprecedented control in an engineered quantum system. We realize a small network of coherently coupled two-level systems with *in-situ* tunable parameters interacting

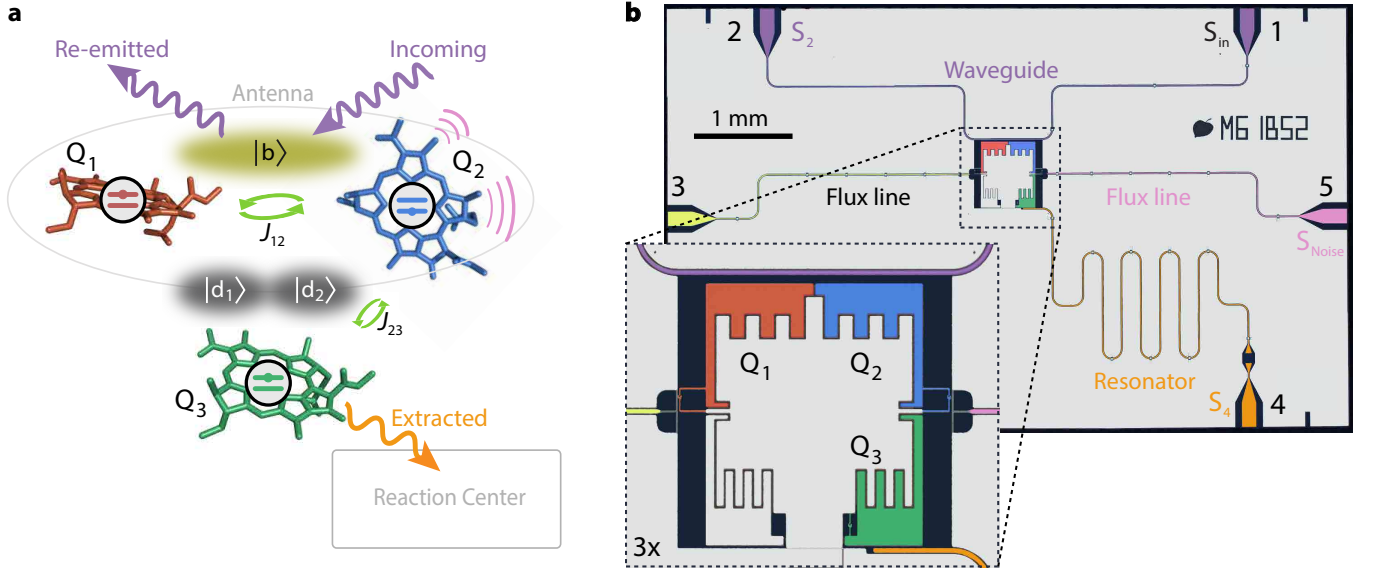


Figure 1: Model system for light-harvesting and its superconducting circuit realization. (a) Schematic of three coupled chlorophyll molecules hosting chromophores modeled as three qubits $Q_{1,2,3}$ (red, blue, green). The strongly coupled Q_1 and Q_2 hybridize with coupling strength J_{12} into a bright state $|b\rangle$ (olive cloud) and dark states (dark gray clouds). Q_2 is coupled to Q_3 with a coupling strength J_{23} which form the dark hybridized states $|d_1\rangle$ and $|d_2\rangle$. The incident, the re-emitted and the harvested radiation are indicated by arrows. Pink lines indicate that Q_2 is subjected to environmental noise. (b) False-color micrograph of the superconducting circuit. Transmon qubits Q_1 and Q_2 (red, blue) are capacitively coupled to a transmission line (purple) and Q_3 (green) is capacitively coupled to a high-emission-rate resonator (orange). Excitation radiation (S_{in}) is applied through port 1 of the transmission line. The re-emitted (S_2) and extracted radiation (S_4) is detected at port 2 and 4, respectively. Low frequency noise with an engineered spectral density, modeling the environment (S_{noise}), is applied to Q_2 via the flux line at port 5.

with an engineered environment, inspired by the proposal of Mostame *et al.*^{26,27}. Superconducting circuits are particularly well suited for this task, since versatile devices can be realized with a high degree of accuracy, and can be controlled and probed experimentally using well developed techniques³.

Here we experimentally investigate energy transport assisted by structured and unstructured environmental noise for coherent and incoherent excitation and demonstrate that its efficiency can approach unity. We also observe static coherences, even under incoherent excitation, and demonstrate good understanding of the full system dynamics.

I. SAMPLE AND SPECTROSCOPIC CHARACTERIZATION

We implement a simplified model of a pigment protein complex consisting of three coupled chlorophyll molecules, labeled $Q_{1,2,3}$ in Fig. 1a. The corresponding Hamiltonian is described in App. H1. This is the smallest system which incorporates all relevant elements, such as excitation trapping, energy mismatch, excitation delocalization, dark and bright states, necessary for studying noise assisted transport^{1,9,11,13–15}. Although current technology allows building larger systems capable of in-

vestigating for example the full FMO complex with 8 sites, we are convinced that it is a necessary first step to explore this novel approach on a simple model system. We realize two-level systems with individually tunable transition frequencies as transmon qubits² in a superconducting circuit (Fig. 1b). The dipole-dipole coupling between molecules Q_1 and Q_2 forms symmetric and antisymmetric, bright $|b\rangle$ and dark $|d\rangle$ state superpositions of the individual qubit excited states $|q_1\rangle$ and $|q_2\rangle$ ^{30–32}. We realize the dipole-dipole interaction by direct capacitive coupling between qubits Q_1 and Q_2 (Fig. 1b). We excite the bright state $|b\rangle$ through an open waveguide to which the two transmon qubits are coupled with equal strength³² modeling the excitation of the antenna part of the photosynthetic complex with photons propagating in free space. A third molecule Q_3 , coupled to Q_2 , acts as a trap for the excitation which is subsequently extracted by transfer to the reaction center. In our circuit, this trapping site is realized as a third qubit which extracts the excitation from the system through its Purcell-like coupling to a transmission line resonator effectively acting as the reaction center. We model the interaction of molecule Q_2 with the environmental vibrational modes of the protein scaffold as fluctuations of its transition frequency. These fluctuations are induced by local magnetic fields acting on Q_2 . While noise can be applied to all qubits, we chose to study local noise, such as the

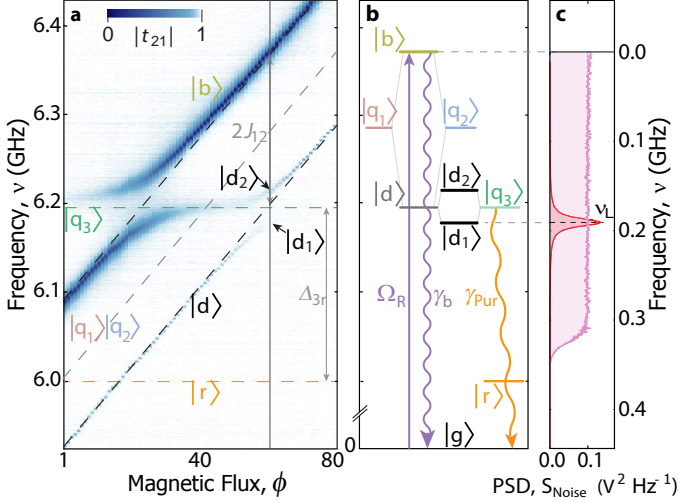


Figure 2: **Measured spectrum, energy levels and applied environmental noise spectra.** (a) Transmission spectra $|t_{21}(\omega)|$ of the three qubit system measured through the transmission line as a function of magnetic flux. Here and in the following, spectral features are labeled by the target state ($|q_1\rangle, |q_2\rangle, |q_3\rangle, |b\rangle, |d\rangle, |d_1\rangle, |d_2\rangle, |r\rangle$) reached in spectroscopic experiments from the ground state $|g\rangle$ of the system. (b) Energy level diagram at the magnetic flux indicated by a gray vertical line in (a). The resonant states $|q_1\rangle$ and $|q_2\rangle$ form bright $|b\rangle$ and dark $|d\rangle$ states. Furthermore, $|q_3\rangle$ is resonant with the $|d\rangle$ state forming $|d_1\rangle$ and $|d_2\rangle$ doublet. Solid downward arrows indicate decay channels, the upward arrow indicates excitation via the waveguide. (c) Measured power spectral density S_{Noise} of the environmental low-frequency noise applied to the flux line of Q_2 . White noise with 325 MHz cutoff is depicted in pink and Lorentzian noise with central frequency ν_L in red.

one induced by a local environment of a pigment protein. When applying noise to several sites we could study the effects correlations in the noise have on the process.

We demonstrate a high degree of tunability of system parameters in a measurement of the frequency-dependent transmission coefficient $|t_{21}(\omega)|$ through the waveguide (see Fig. 2a) keeping the transition frequency of Q_3 fixed at $\omega_3/2\pi = 6.198$ GHz and linearly sweeping the transition frequencies of Q_1 and Q_2 maintaining $\omega_1 = \omega_2$. We tune the qubit transition frequencies by magnetic fields applied using a coil and two flux lines shorted close to the SQUID loops of transmon qubits Q_1 and Q_2 (see App. A). In this measurement, we observe that Q_1 and Q_2 form bright and dark states ($|b\rangle, |d\rangle$) with frequencies ω_b and ω_d separated by $2J_{12}/2\pi = 173.4$ MHz (see App. B). The bright state linewidth $\gamma_b/2\pi = 12.4$ MHz is consistent with the sum of the individual qubit radiative linewidths $\gamma_1/2\pi = 7.39$ MHz and $\gamma_2/2\pi = 6.57$ MHz dominated by the coupling to the waveguide. This indicates superradiance of the coupled two qubit system^{32,33}. The subradiant dark state $|d\rangle$ has a narrow linewidth of $\gamma_d/2\pi = 0.29$ MHz limited by the residual asymmetry in

Q_1 and Q_2 parameters (see App. A) with a bright to dark state linewidth ratio of $\gamma_b/\gamma_d \approx 43$. Dark states have been suggested to improve the efficiency of biologically inspired photocells by protecting the excitation from re-emission^{14,34}. For $\omega_1/2\pi = \omega_2/2\pi = 6.285$ GHz (solid vertical line in Fig. 2a) the dark state $|d\rangle$ coherently hybridizes with $|q_3\rangle$ forming a doublet $|d_1\rangle$ and $|d_2\rangle$ split by $2J_{d3}/2\pi = 37$ MHz consistent with the individual qubit couplings (see Fig. 2b and App. A). We detune ω_3 from the fixed frequency $\lambda/2$ resonator state $|r\rangle$ at $\omega_r/2\pi = 6.00$ GHz by $\Delta_{3r} = \omega_3 - \omega_r$. This sets the radiative Purcell decay rate⁸ $\gamma_{\text{Pur}}/2\pi \approx 20$ MHz of Q_3 (see App. C) effectively modeling the energy extraction rate at the reaction center. As desired, all relevant microwave frequency system parameters are consistently scaled by a factor of $\sim 10^5$ relative to the optical frequency energy scales of the FMO complex²⁶.

II. EXCITATION TRANSFER WITH UNIFORM WHITE NOISE

To study energy transfer through the circuit we tune Q_1 and Q_2 into resonance to form bright and dark states at frequencies $\omega_b/2\pi = \nu_b = 6.371$ GHz and $\omega_d/2\pi = 6.198$ GHz. Qubit Q_3 is tuned into resonance with the dark state $\omega_3 = \omega_d$ creating two resonances at $\omega_{d1}/2\pi = \nu_{d1} = 6.179$ GHz and $\omega_{d2}/2\pi = \nu_{d2} = 6.216$ GHz. We coherently excite the bright state $|b\rangle$ through port 1 of the device with a continuous tone at frequency ω_b and amplitude corresponding to a bright state Rabi frequency of $\Omega_R/2\pi = 14$ MHz (see App. D). We measure the power spectral density (PSD) $S_2(\omega)$ of the photons scattered along the waveguide into port 2 of the device characterizing the re-emission from the absorption site. $S_2(\omega)$ displays a narrow coherent peak at ω_b due to elastically (Rayleigh) scattered photons and a broad resonance fluorescence spectrum with a width given by γ_b due to the inelastically scattered photons (bottom purple line in Fig. 3a). With increasing drive amplitude we observe a bright state Mollow triplet³², see Fig. S4. Due to the energy mismatch of the bright state $|b\rangle$ and the dark state doublet ($|d_1\rangle, |d_2\rangle$) no excitations are transferred to qubit Q_3 and thus no photons are detected at the resonator port 4, as shown by the vanishing PSD $S_4(\omega)$ at $\Phi_W^2 = 0$ pWb² (bottom orange line in Fig. 3a). In our model system, no energy is transferred from the antenna to the reaction center in the absence of environmental noise.

To engineer a broad environmental noise spectrum, such as the one generated by the combination of background thermal noise and overlapping vibrational modes of the protein scaffold present in light harvesting systems²⁶, we apply white Gaussian noise to port 5 inducing frequency fluctuations in Q_2 . The broad Markovian noise has a power spectral density of adjustable amplitude, constant up to a cutoff frequency of 325 MHz,

characterized by its integrated flux noise power Φ_W^2 at qubit Q_2 (see App. E and Fig. 2c). We note that applying synthesized noise to $|q_2\rangle$ effectively creates a classical environment that can be described by the Haken-Strobl-Reineker model^{36,37} for white noise. Applying classical, as opposed to quantum noise, offers a unique possibility to engineer noise with controllable power spectral density capable of creating environments that approximate those of pigment-protein complexes²⁶ without increasing complexity of the device design.

Even for small applied noise power we observe energy transfer from the bright $|b\rangle$ to the dark state doublet $|d_1\rangle, |d_2\rangle$ indicated by two resonances at frequencies ω_{d1} and ω_{d2} in the detected PSD $S_4(\omega)$ (orange line at $\Phi_W^2 = 0.1 \text{ pWb}^2$ in Fig. 3a). The excitation transport is enabled by those frequency components of the noise spectrum that bridge the energy difference $2J_{12} \pm J_{d3}$ between bright $|b\rangle$ and dark states $|d_1\rangle, |d_2\rangle$. We have verified this aspect by reducing the bandwidth of the noise to below that energy difference in which case no energy transfer is observed. The emission linewidths, i.e. the emission rates of $|d_1\rangle$ and $|d_2\rangle$ into the resonator are determined by the Purcell decay rate γ_{pur} (see App. C). The well resolved doublet in the detected spectrum $S_4(\omega)$ indicates that static coherences of the underlying quantum network are observable in noise induced transport. Based on the observations of the doublet, we expect beatings with frequency $2J_{d3}$ to be observable in temporally resolved measurements of the power at the extraction site.

With increasing applied noise power Φ_W^2 , the power spectrum $S_2(\omega)$ of the resonance fluorescence of the bright state $|b\rangle$ broadens due to the pure dephasing induced by the noise. From this measurement we determine the bright state pure dephasing rate γ_ϕ^b in dependence on the applied white noise power Φ_W^2 (see App. F). The extracted power $S_4(\omega)$ first increases with increasing noise power Φ_W^2 while the doublet remains resolved. At noise powers above $\Phi_W^2 \approx 2 \text{ pWb}^2$ the observed doublet transforms into a single resonance marking a crossover from the strong-coupling regime ($2J_{d3} \gtrsim \gamma_\phi^b$) to the weak-coupling regime ($2J_{d3} \lesssim \gamma_\phi^b$) where the remaining resonance stems from the incoherently excited $|q_3\rangle$ state (see App. G). Beyond this threshold, the extracted power decreases. For this simple situation of only three sites and Markovian noise, all essential features of the experimentally observed power spectra are consistent with both Lindblad master equation and Bloch-Redfield calculations (see Fig. 3b and App. H).

Integrating the measured power spectral densities $S_4(\omega)$ and $S_2(\omega)$ while omitting contributions from elastic (Rayleigh) scattering, we find that the total power re-emitted from the bright state into the waveguide in forward direction P_2 decreases monotonically as a function of applied noise power Φ_W^2 (open purple squares in Fig. 4a). In contrast, the total power detected at the extraction site P_4 first increases rapidly with Φ_W^2 , exhibits a pronounced maximum and then decreases again (open orange diamonds in Fig. 4a). The increase for small de-

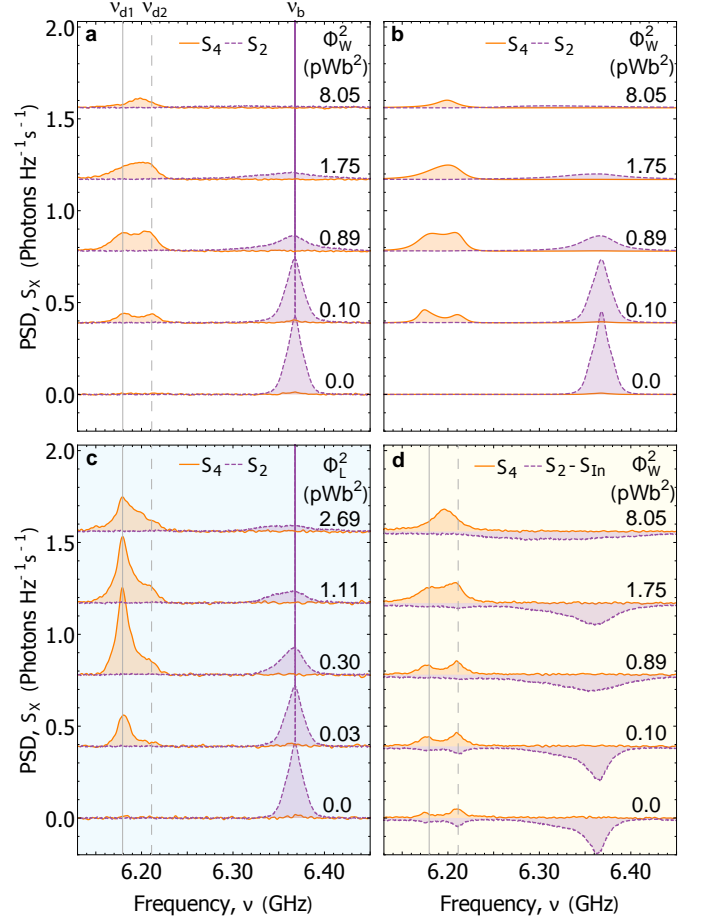


Figure 3: **Measured power spectral densities (PSD)** of radiation extracted from the resonator $S_4(\omega)$ (solid orange lines) and re-emitted into the transmission line $S_2(\omega)$ (dashed purple lines) for coherent excitation as a function of (a) white noise power Φ_W^2 and (c) Lorentzian noise power Φ_L^2 . (b) Master equation calculations of $S_4(\omega)$ and $S_2(\omega)$ for coherent excitation as a function of Φ_W^2 . (d) Measured PSD for incoherent excitation as a function of Φ_W^2 . Dashed purple lines indicate the reduction of the measured PSD in incoherent microwave radiation S_{in} , due to energy transfer through the system. PSD for different noise powers are displaced by $0.2 \text{ Photons s}^{-1} \text{Hz}^{-1}$.

phasing rates is a consequence of noise-induced incoherent transitions between bright and dark states^{14,38} allowing the system to overcome the energy mismatch.

From the integrated powers we calculate the transfer efficiency of the excitation from the absorption site to the extraction site as $\eta = P_4/(P_4 + 2P_2)$. The factor 2 accounts for the bidirectional character of the bright state resonance fluorescence³², i.e. equal powers are emitted in forward and backward direction, while we detect only in forward direction. The transport efficiency η (green circles in Fig. 4a) shows a rapid increase from zero, a broad maximum of $\eta_W^{\text{max}} = 39\%$ and then a slow decrease with increasing pure dephasing rate γ_ϕ^b (see top axis in Fig. 4a), which are the characteristic features of noise as-

sisted transport^{8–10}. The decrease in efficiency above an optimal noise power is due to dephasing-induced population localization, also referred to as the quantum Zeno effect^{8–10}.

The measured integrated powers and hence the efficiency are in good agreement with results from master equation simulations (solid lines in Fig. 4a). Using rate equations (see App. H3) we show that the maximal efficiency is $\eta_W^{\max} \approx (1 - \gamma_b/\gamma_{\text{Pur}})$ approaching 100% for $\gamma_b \ll \gamma_{\text{Pur}}$. Although small γ_b maximizes the transfer efficiency¹⁰, the total extracted power at optimal applied noise is proportional to γ_b . Therefore for practical light harvesting applications one may choose to maximize output power while compromising on efficiency^{14,38}. Similarly, we have not chosen a smaller γ_b in our experiment to maximize the efficiency, but opted for a larger extracted power to achieve a high signal-to-noise ratio at an acceptable integration time. Finally, we note that in our data the maximum efficiency η_W^{\max} occurs at the strong-to-weak coupling crossover $2J_{d3} \approx \gamma_\phi^b$. At this point, the transfer rate γ_ϕ^b between $|b\rangle$ and $|d\rangle$ is comparable to the transfer rate between $|d\rangle$ and $|q_3\rangle$, which is approximately given by $2J_{d3}^2/\gamma_\phi^b$ (see App. H3). This experimentally demonstrates the interplay between quantum coherent effects and classical dephasing enhancing excitation transport.

III. EXCITATION TRANSFER WITH LORENTZIAN ENVIRONMENT

It has been conjectured that structured environmental noise, such as the one originating from long lived vibrational modes of chlorophyll molecules in photosynthetic complexes, can further enhance the energy transfer efficiency between the disordered molecular sites of the network in a scenario known as the phonon antenna mechanism^{1,12}. To demonstrate this concept, we apply environmental noise with Lorentzian PSD, characterized by its central frequency ν_L , its width $\Delta\nu_L$ and amplitude (Fig. 2c), to qubit Q_2 . We select a fixed bandwidth $\Delta\nu_L = 10$ MHz which in good approximation corresponds to the scaled linewidth of the environmental noise expected from vibrational modes in natural photosynthetic complexes^{15,26}. Since $\Delta\nu_L$ is comparable to the decay rates γ_b and γ_{Pur} the spectral properties of the noise effectively create a non-Markovian environment. Initially, we choose the Lorentzian central frequency $\nu_L = 190$ MHz to be resonant with the $|b\rangle$ to $|d_1\rangle$ frequency difference $\Delta_{b,d1}$. The qualitative features of the measured power spectral densities $S_2(\omega)$ and $S_4(\omega)$ and their dependence on the integrated applied noise power Φ_L^2 (Fig. 3c) are comparable to the white noise case (Fig. 3a) with some distinct differences. As a direct consequence of applying Lorentzian noise resonant at $\Delta_{b,d1}$, $S_4(\omega)$ exhibits a strong resonance exactly at ω_{d1} and a weaker resonance at ω_{d2} . The excitation

transfer can be interpreted as a two-photon process³⁹ absorbing one photon from the coherent excitation field at frequency ω_b and emitting one photon into the environmental noise field at frequency $\Delta_{b,d1}$ or $\Delta_{b,d2}$. This effectively creates a transition from the joint ground state through the bright state $|b\rangle$ into the dark states $|d_1\rangle$ or $|d_2\rangle$ from which energy is extracted.

When we sweep the Lorentzian noise center frequency over a broad range from $\nu_L = 0$ to 300 MHz at weak noise power $\Phi_L^2 = 0.016$ pWb², we observe two well resolved maxima in transferred power P_4 when the noise is resonant with the bright to dark state frequency differences $\Delta_{b,d1}$ and $\Delta_{b,d2}$ (Fig. S8). In contrast, no energy transfer is observed when the noise is far detuned. Both observations clearly demonstrate the strong sensitivity of the energy transfer on the spectral properties of the environmental noise and indicate that the noise assisted transport is enabled by a narrow part of the noise PSD that matches the energy gap otherwise blocking the energy transfer in the system. This observation is consistent with stochastically averaged master equation simulations (see Fig. S9 and App. H5). We note that despite applying classical noise the dynamics induced by Lorentzian environment cannot be simulated with the HSR approach or even its extension for colored noise^{40,41}, due to its strong non-Markovian character. Therefore, a full quantum numerical simulation is required at the cost of significant computational effort.

For Lorentzian environmental noise, the integrated detected powers also display the characteristic properties of noise assisted transport as a function of Φ_L^2 (Fig. 4b) as discussed before for white noise (Fig. 4a). However, we note that the extracted power P_4 is almost twice as large at the same bright state excitation amplitude (Fig. 4a,b) leading to increased maximal efficiency $\eta_L^{\max} = 58\%$. This indicates that structured environmental noise matching internal energy differences of the quantum network indeed enhances the efficiency of the energy transfer. Estimating the effective qubit-environment coupling constant K (see Fig. 4b and App. I) we observe that the maximum in efficiency coincides with $K/2\pi \approx 100$ MHz which is comparable to the inter-qubit coupling constant J_{12} . This demonstrates that strong coupling between qubit and phononic modes is required to achieve maximal energy transport. Such a situation has been suggested to enhance the transport in cyanobacterial light-harvesting proteins, allophycocyanin and C-phycocyanin⁴².

We have also applied a coherent tone with controlled frequency ν_c and amplitude to qubit Q_2 through the environmental channel (port 5) (see App. J) and observe even larger extracted powers at the same bright state $|b\rangle$ input field amplitude and near unit transfer efficiency (see Fig. S10c). While this case does not occur in natural light harvesting since the environment cannot be fully coherent, it represents an interesting limiting case. In natural light harvesting systems exposed to incoherent environments, the highest transfer efficiency is realized

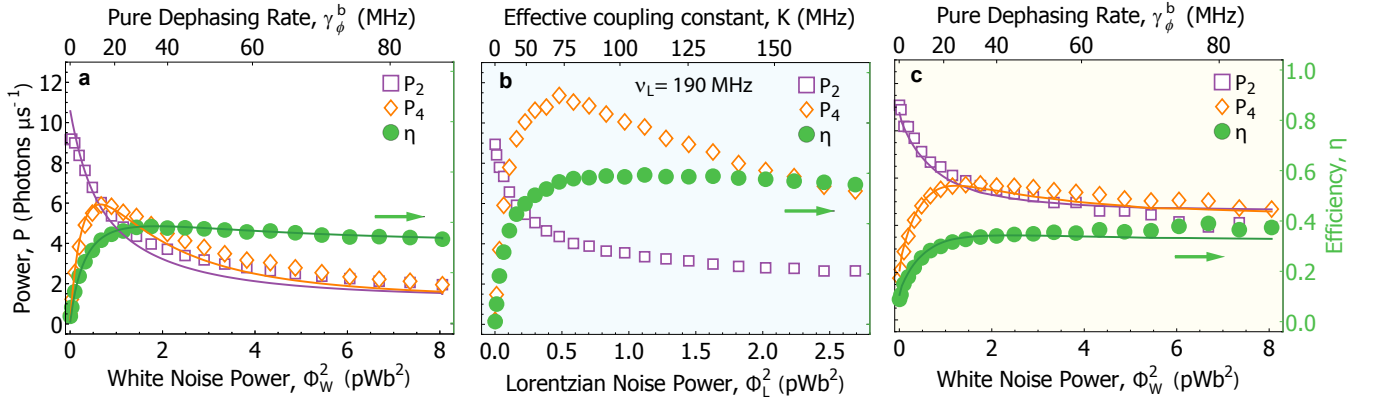


Figure 4: **Total extracted power P_4 (orange diamonds), re-emitted power P_2 (purple squares) and transport efficiency η (green circle)** for (a) coherent excitation and white noise environments, (b) coherent excitation and Lorentzian noise environments and (c) incoherent excitation and white noise environments. Data is plotted as a function of white noise power Φ_W^2 or equivalently bright state dephasing rate γ_ϕ^b for (a) and (c) and as a function of Lorentzian noise power Φ_L^2 or equivalently effective qubit-environment coupling constant K for (b). Solid lines are results of master equation simulations (see App. H 2).

for structured environmental noise with a narrow spectral density peaked at the frequency of the internal energy mismatch between the sites of the network. Any excess spectral width of the environmental noise leads to additional dephasing (see App. H 4), which in turn reduces the absorption and energy transfer efficiency. These aspects are clearly demonstrated by the presented set of experiments comparing energy transfer with white and Lorentzian noise spectral density.

IV. INCOHERENT EXCITATION

In the final set of experiments we excite the qubit system with incoherent microwave radiation to mimic excitation of biological pigment protein complexes with sunlight. We engineer 0.95 GHz broad incoherent microwave radiation centered at ω_B that spans over all qubit transition frequencies (see App. K 1). The incoherent microwave power integrated over the bright state spectrum was adjusted to be equal to the drive power used for the case of coherent excitation. In this experiment we study the transport of incoherently created excitations as a function of applied white noise power.

Since it is not possible to distinguish between the broad incoming incoherent and the re-emitted radiation at port 2 we plot in Fig. 3d the difference between detected power spectrum S_2 at port 2 and the separately measured incoherent radiation spectrum S_{In} . The difference spectrum corresponds to the sum of the absorbed and the re-emitted spectrum \hat{S}_2 .

When increasing the applied white noise power we observe that $S_4(\omega)$ and $[S_2(\omega) - S_{\text{In}}(\omega)]$ show general features (Fig. 3d) similar to the ones observed for coherent

excitation. However, in case of incoherent excitation a finite power ($P_4 = 0.9 \text{ Photons } \mu\text{s}^{-1}$) is extracted at port 4 even in the absence of applied environmental white noise ($\Phi_W^2 = 0$). The observed extracted power is a result of direct excitation of the dark state, due to its finite coupling to the open waveguide. When the dark state is not completely dark simultaneous incoherent excitation of bright and dark states reduces coherence between Q_1 and Q_2 and therefore increases dephasing of the system. Existence of dark states in photosynthetic complexes can therefore help protect the system against dephasing induced by incoherent excitation. The observation of the $|d_1\rangle, |d_2\rangle$ doublet in $S_2(\omega)$ (Fig. 3d) demonstrates that static coherences can be observed for incoherent excitation, i.e. even in the absence of coherent sources, as long as the coherent coupling between the sites is larger than the total dephasing.

The maximum of the measured efficiency $\eta_{\text{W,inc}}^{\text{max}} = 38\%$ is smaller but comparable to the case of coherent excitation with the maximum shifted towards higher applied environmental white noise powers. Comparable efficiencies are consistent with rate equation descriptions where the efficiency is independent of the spectral and coherence properties of the excitation. On the other hand, the extracted power P_4 is by more than a factor 2 larger at the highest environmental noise power ($\Phi_W^2 = 8.05 \text{ pWb}^2$) compared to the coherent excitation case. This indicates that absorption of the incoherent photons is not as strongly affected by environmental dephasing as for coherent excitation, due to a persistent overlap between broadened bright state spectrum and spectrum of the incoherent irradiation. Similar conclusion can be made for energy transport induced by Lorentzian noise for incoherent excitation (see App. K 2).

V. CONCLUSIONS

In a proof of concept experiment we studied models of photosynthetic processes using superconducting quantum circuits. With a system of three coupled qubits we demonstrated how the interplay of quantum coherence and environmental interactions affects energy transport in a system with excellent control achievable over all relevant parameters. We expect this approach to be extensible to study other relevant aspects of light harvesting, such as time-resolved dynamics of the coherent excitation transfer; the role of quantum environments realizable in electronic circuit models as low frequency quantum harmonic oscillators^{14,26}; and scaling to systems with a larger number of coherent sites such as the FMO complex. Furthermore, we expect similar approaches to be applicable not only to study light-harvesting processes but also other interesting aspects of quantum biology such as the sense of smell in animals and humans and magneto reception in birds^{1,2}. It could also be interesting to evaluate the potential of the techniques presented here to model processes in quantum chemistry and search for potential future applications of related methods to support, for example, the design of catalysts, e.g. for nitrogen fixation, or bio-molecular compounds for drug development.

Acknowledgements We are grateful to G. Blatter and D. Vion for helpful feedback on the manuscript and T.

Walter and P. Kurpiers for valuable discussions. Work of H.E.T. and S.K. was supported by the US Department of Energy, Office of Basic Energy Sciences, Division of Materials Sciences and Engineering, under Award No. DE-SC0016011. A.W.C. and F.A.Y.N.S. acknowledge support from the Winton Programme for the Physics of Sustainability. F.A.Y.N.S. also acknowledges support by the Engineering and Physical Sciences Research Council (EPSRC). Work of A.P., A.B., M.C., S.G., Y.S., C.E. and A.W. was supported by ETH Zürich.

Competing Interests The authors declare that they have no competing financial interests.

Correspondence Correspondence and requests for materials should be addressed to A.P. (email: anton.potocnik@phys.ethz.ch).

Author Contributions AP, AB and MCC designed the sample, performed the experiment and analyzed the data. SG fabricated the sample. The FPGA firmware was implemented by YS. FAYNS, CC and AWC performed numerical simulations with the uniform environment and contributed to the experimental set-up. SAK and HET performed numerical simulations with the structured environment. AP and AW co-wrote the manuscript. CE commented on the manuscript. All authors contributed to the manuscript preparation. The project was led by AP and AW.

* These authors contributed equally to this work

¹ Huelga, S. F. & Plenio, M. B. Vibrations, quanta and biology. *Contemp. Phys.* **54**, 181–207 (2013).

² Lambert, N. *et al.* Quantum biology. *Nature Phys.* **9**, 10–18 (2013).

³ Scholes, G. D. *et al.* Using coherence to enhance function in chemical and biophysical systems. *Nature* **543**, 647–656 (2017).

⁴ Engel, G. S. *et al.* Evidence for wavelike energy transfer through quantum coherence in photosynthetic systems. *Nature* **446**, 782–786 (2007).

⁵ Collini, E. *et al.* Coherently wired light-harvesting in photosynthetic marine algae at ambient temperature. *Nature* **463**, 644–647 (2010).

⁶ Panitchayangkoon, G. *et al.* Long-lived quantum coherence in photosynthetic complexes at physiological temperature. *Proc. Natl. Acad. Sci. U.S.A.* **107**, 12766–12770 (2010).

⁷ Förster, T. 10th Spiers Memorial Lecture. Transfer mechanisms of electronic excitation. *Faraday Discuss.* **27**, 7–17 (1959).

⁸ Olaya-Castro, A., Lee, C. F., Olsen, F. F. & Johnson, N. F. Efficiency of energy transfer in a light-harvesting system under quantum coherence. *Phys. Rev. B* **78**, 085115 (2008).

⁹ Plenio, M. B. & Huelga, S. F. Dephasing-assisted transport: quantum networks and biomolecules. *New J. Phys.* **10**, 113019 (2008).

¹⁰ Rebentrost, P., Mohseni, M., Kassal, I., Lloyd, S. & Aspuru-Guzik, A. Environment-assisted quantum transport. *New J. Phys.* **11**, 033003 (2009).

¹¹ Caruso, F., Chin, A. W., Datta, A., Huelga, S. F. & Plenio, M. B. Highly efficient energy excitation transfer in light-harvesting complexes: The fundamental role of noise-assisted transport. *J. Chem. Phys.* **131**, 105106 (2009).

¹² Chin, A. W., Huelga, S. F. & Plenio, M. B. Coherence and decoherence in biological systems: principles of noise-assisted transport and the origin of long-lived coherences. *Phil. Trans. R. Soc. A* **370**, 3638–3657 (2012).

¹³ Chin, A. W. *et al.* The role of non-equilibrium vibrational structures in electronic coherence and recoherence in pigment-protein complexes. *Nature Phys.* **9**, 113–118 (2013).

¹⁴ Creatore, C., Parker, M. A., Emmott, S. & Chin, A. W. Efficient Biologically Inspired Photocell Enhanced by Delocalized Quantum States. *Phys. Rev. Lett.* **111**, 253601 (2013).

¹⁵ Rey, M. d., Chin, A. W., Huelga, S. F. & Plenio, M. B. Exploiting structured environments for efficient energy transfer: The phonon antenna mechanism. *J. Phys. Chem. Lett.* **4**, 903–907 (2013).

¹⁶ Imada, H. *et al.* Real-space investigation of energy transfer in heterogeneous molecular dimers. *Nature* **538**, 364 (2016).

¹⁷ Viciani, S., Lima, M., Bellini, M. & Caruso, F. Observa-

- tion of Noise-Assisted Transport in an All-Optical Cavity-Based Network. *Phys. Rev. Lett.* **115**, 083601 (2015).
- ¹⁸ Viciani, S., Gherardini, S., Lima, M., Bellini, M. & Caruso, F. Disorder and dephasing as control knobs for light transport in optical fiber cavity networks. *Sci. Rep.* **6**, 37791 (2016).
 - ¹⁹ Biggerstaff, D. N. *et al.* Enhancing coherent transport in a photonic network using controllable decoherence. *Nat. Commun.* **7**, 11282 (2016).
 - ²⁰ León-Montiel, R. d. J. *et al.* Noise-assisted energy transport in electrical oscillator networks with off-diagonal dynamical disorder. *Sci. Rep.* **5**, 17339 (2015).
 - ²¹ Park, J. & Lee, S. Quantum nonsignaling-assisted zero-error classical capacity of qubit channels. *Phys. Rev. A* **93**, 032334 (2016).
 - ²² Hemmig, E. A. *et al.* Programming Light-Harvesting Efficiency Using DNA Origami. *Nano Lett.* **16**, 2369–2374 (2016).
 - ²³ Harris, N. C. *et al.* Quantum transport simulations in a programmable nanophotonic processor. *Nat Photon* **11**, 447–452 (2017).
 - ²⁴ Schmidt, S. & Koch, J. Circuit qed lattices: Towards quantum simulation with superconducting circuits. *Ann. Phys. (Berlin)* **525**, 395–412 (2013).
 - ²⁵ Houck, A. A., Türeci, H. E. & Koch, J. On-chip quantum simulation with superconducting circuits. *Nat. Phys.* **8**, 292–299 (2012).
 - ²⁶ Mostame, S. *et al.* Quantum simulator of an open quantum system using superconducting qubits: exciton transport in photosynthetic complexes. *New J. Phys.* **14**, 105013 (2012).
 - ²⁷ Mostame, S. *et al.* Emulation of complex open quantum systems using superconducting qubits. *Quantum Inf. Process.* **16**, 44 (2017).
 - ²⁸ da Silva, M. P., Bozyigit, D., Wallraff, A. & Blais, A. Schemes for the observation of photon correlation functions in circuit QED with linear detectors. *Phys. Rev. A* **82**, 043804–12 (2010).
 - ²⁹ Koch, J. *et al.* Charge-insensitive qubit design derived from the Cooper pair box. *Phys. Rev. A* **76**, 042319 (2007).
 - ³⁰ May, V. & Kühn, O. *Charge and Energy Transfer Dynamics in Molecular Systems* (Wiley-VCH, 2004).
 - ³¹ Ferretti, M. *et al.* Dark states in the light-harvesting complex 2 revealed by two-dimensional electronic spectroscopy. *Sci. Rep.* **6**, 20834 (2016).
 - ³² van Loo, A. *et al.* Photon-mediated interactions between distant artificial atoms. *Science* **342**, 1494–1496 (2013).
 - ³³ Mlynek, J., Abdumalikov, A., Eichler, C. & Wallraff, A. Observation of dicke superradiance for two artificial atoms in a cavity with high decay rate. *Nat. Commun.* **5**, 5186 (2014).
 - ³⁴ Dong, H., Xu, D.-Z., Huang, J.-F. & Sun, C.-P. Coherent excitation transfer via the dark-state channel in a bionic system. *Light Sci. Appl.* **1**, e2 (2012).
 - ³⁵ Sete, E. A., Gambetta, J. M. & Korotkov, A. N. Purcell effect with microwave drive: suppression of qubit relaxation rate. *Phys. Rev. B* **89**, 104516 (2014).
 - ³⁶ Haken, H. & Reineker, P. The coupled coherent and incoherent motion of excitons and its influence on the line shape of optical absorption. *Zeitschrift für Physik* **249**, 253–268 (1972).
 - ³⁷ Haken, H. & Strobl, G. An exactly solvable model for coherent and incoherent exciton motion. *Z. Phys. A: Hadrons Nucl.* **262**, 135–148 (1973).
 - ³⁸ Fruchtmann, A., Gomez-Bombarelli, R., Lovett, B. W. & Gauger, E. M. Photocell optimization using dark state protection. *Phys. Rev. Lett.* **117**, 203603 (2016).
 - ³⁹ Li, J. *et al.* Motional averaging in a superconducting qubit. *Nat. Commun.* **4**, 1420 (2013).
 - ⁴⁰ Warns, C., Barvik, I. & Reineker, P. Energy transport and optical line shapes in dimers: Analytical description of the influence of colored noise. *Phys. Rev. E* **57**, 3928 (1998).
 - ⁴¹ Barvák, I., Warns, C., Neidlinger, T. & Reineker, P. Erratum to: Simulation of excitonic optical line shapes of cyclic molecular aggregates with 9 and 18 units: influence of quasi-static and dynamic disorder. *Chem. Phys.* **255**, 403–405 (2000).
 - ⁴² Womick, J. M. & Moran, A. M. Vibronic Enhancement of Exciton Sizes and Energy Transport in Photosynthetic Complexes. *J. Phys. Chem. B* **115**, 1347–1356 (2011).

Appendix

Contents

A. Sample and Experimental Setup	7
B. Description of Symmetric and Antisymmetric superposition of Q_1 and Q_2	9
C. Characterization of Q_3 and its Purcell Decay	10
D. Rabi Rate and PSD Calibration	11
E. Noise Generation	12
F. Pure Dephasing Rate Calibration	12
G. White Noise PSD Analysis	12
H. Theoretical Description	13
1. Master Equation	13
2. Simulations	14
3. Rate Equations	14
4. Dephasing Rate due to Lorentzian Noise	15
5. Simulations with Lorentzian Noise	17
I. Effective Qubit-Environment coupling	18
J. Modulating the Transition Frequency of Q_2 with a Coherent Tone	18
K. Excitation with Incoherent Microwave Radiation	19
1. Engineering Incoherent Radiation	19
2. Incoherently Excited System Subject to Lorentzian Noise	19
References	20

Appendix A: Sample and Experimental Setup

The three qubits are implemented with a grounded design, similar to X-mon qubits¹, to minimize the unwanted capacitive coupling between Q_1 and Q_3 . Their arrangement (see Fig. 1b in the main text) yields capacitive coupling rates of $J_{12}/2\pi = 83.6$ MHz, $J_{23}/2\pi = 33.4$ MHz and an order of magnitude smaller $J_{13}/2\pi = 3.67$ MHz. All reported qubit parameters are determined at the qubit transition frequency of $\omega/2\pi = 6.28$ GHz. When extracting individual qubit parameters the other two qubits are detuned by at least 1.5 GHz. The measured maximum transition frequencies between the ground $|g\rangle$ and first excited state $|e\rangle$ are $\omega_1^{\max}/2\pi = 6.948$ GHz, $\omega_2^{\max}/2\pi = 6.694$ GHz and $\omega_3^{\max}/2\pi = 7.271$ GHz

for the three qubits and their anharmonicities of the first-to-second excited state are $\alpha_1/2\pi = -140$ MHz, $\alpha_2/2\pi = -142$ MHz and $\alpha_3/2\pi = -137$ MHz. The spectroscopically measured pure dephasing rates of Q_1 and Q_2 are $\gamma_\phi^{(1)}/2\pi = 115$ kHz and $\gamma_\phi^{(2)}/2\pi = 82$ kHz. Q_1 and Q_2 are coupled to an open waveguide (transmission line) with coupling rates $\gamma_1/2\pi = 6.57$ MHz and $\gamma_2/2\pi = 7.39$ MHz. Q_3 is coupled to a $\lambda/2$ resonator with coupling coefficient $g/2\pi \approx 90$ MHz. The uncoupled resonator has a fundamental frequency of $\omega_r/2\pi = 6.00$ GHz and a loaded quality factor of $Q_L \approx Q_{\text{ext}} \approx 55$ dominated by the external coupling. The transition frequencies of the three qubits are tuned by magnetic flux Φ_i ,²

$$\omega_i(\Phi_i) \simeq (\omega_i^{\max} - \alpha_i) \sqrt{|\cos(\pi\Phi_i/\Phi_0)|} + \alpha_i, \quad (\text{A1})$$

where Φ_0 is the flux quantum, for $i = 1 - 3$ qubits. Magnetic flux is generated by applying DC currents to two flux lines (FL1, FL2) located close to the SQUID loops of Q_1 and Q_2 and to a superconducting coil coupled globally to all three qubits. Individual qubit frequency control is obtained by inverting the flux coupling matrix and applying appropriate currents.

Coherent microwave radiation (RF) generated at room temperature by a commercial source is thermalized and attenuated at the 4 K, 100 mK and 11 mK stages of dilution refrigerator and applied to the sample at port 1 of the waveguide (see schematic diagram in Fig. S1). Radiation emitted from the waveguide and from the resonator is amplified with high-electron-mobility transistor (HEMT) amplifiers at 4 K followed by a chain of ultralow-noise (ULN) and low-noise (LN) amplifiers at room temperature. Three isolators are inserted between the sample and the HEMT amplifier to suppress the amplifier input noise propagating back to the sample. The radiation emitted from port 2 of the waveguide is filtered with a band-pass filter (BPF). The amplified signals are down-converted to an intermediate frequency (IF) of 250 MHz with an IQ mixer using a local oscillator (LO) tone and then digitized with an analog-to-digital converter (ADC). The digital signal in the measurement bandwidth of 250 MHz is then processed by a field-programmable-gate-array (FPGA) which determines the amplitude and the power spectral density of the signal³. Typically $2^{24} \approx 16 \cdot 10^6$ samples are collected in about 15 min to obtain a single power spectral density $S(\omega)$ measurement. The low frequency noise is generated by an arbitrary waveform generator (AWG) and combined with the DC bias using a bias tee with a low-frequency cutoff of 5 kHz and then applied to FL2 (see Fig. S1). Instead of an AWG we could use, for example, a heated resistor to generate low frequency white noise. However, AWG offers a unique advantage of *in-situ* control of both amplitude and shape of the noise

with detuning $\Delta = \omega_i - \omega_{\text{in}}$, excitation frequency ω_{in} and Rabi rate Ω_{R} . From the fit we extract the radiative decay rate γ_{r} , dominated by the coupling rate to the waveguide, and the pure dephasing rate γ_{ϕ} for both states. Here we neglect the non-radiative decay. We find a higher frequency bright state coupling rate of $\gamma_{\text{b}}/2\pi = 12.44$ MHz and pure dephasing rate of $\gamma_{\phi}^{\text{b}}/2\pi = 0.38$ MHz and a lower frequency subradiant state coupling rate of $\gamma_{\text{a}}/2\pi = 0.29$ MHz and comparable pure dephasing rate of $\gamma_{\phi}^{\text{d}}/2\pi = 0.55$ MHz.

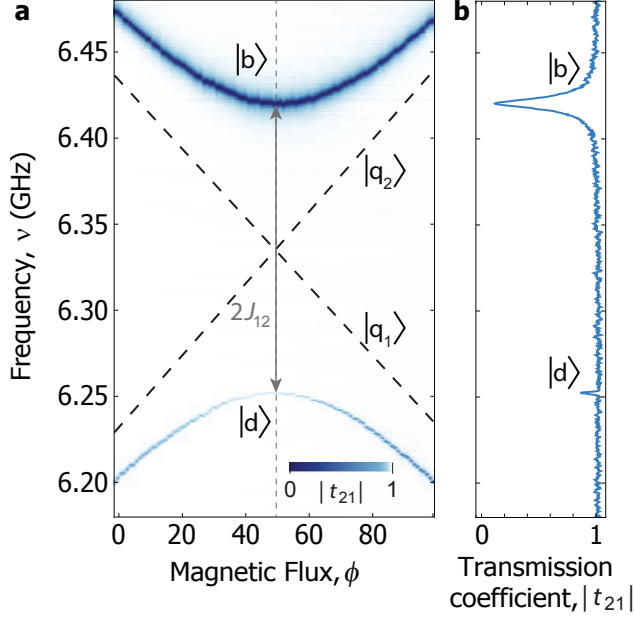


Figure S2: **Q₁, Q₂ avoided crossing.** (a) Measured frequency dependent transmission coefficient $|t_{21}|$ of the waveguide as a function of magnetic flux. $|q_1\rangle$ and $|q_2\rangle$ transition frequencies linearly cross (black dashed lines). $|q_3\rangle$ is detuned by more than 1.5 GHz. (b) $|t_{21}|$ measurement as a function of frequency ν at $\phi = 49$ [vertical dashed line in (a)] where $|q_1\rangle$ and $|q_2\rangle$ are maximally hybridized.

Appendix C: Characterization of Q₃ and its Purcell Decay

We tune the Q₃ decay rate by adjusting the $|q_3\rangle$ transition frequency detuning from the extraction resonator frequency. When the resonator decay rate is large, the radiative decay rate of the qubit is enhanced by the Purcell effect^{6,7}. The Purcell decay rate⁸

$$\gamma_{\text{Pur}} = \frac{\kappa}{2} - \frac{\sqrt{2}}{2} \sqrt{-A + \sqrt{A^2 + (\kappa\Delta_{3r})^2}}, \quad (\text{C1})$$

with $A = \Delta_{3r}^2 + 4g^2 - \kappa^2/4$, depends on the coupling g between the qubit and the resonator, the resonator decay rate κ and the detuning Δ_{3r} between the qubit and the resonator. In the dispersive limit ($\Delta_{3r} \gg g$), Eq. (C1) reduces to the well known expression $\gamma_{\text{Pur}} = \kappa(g/\Delta_{3r})^2$ ^{2,8}. The Purcell broadening of the Q₃ spectral line is observed in a reflection coefficient measurement $|t_{44}|$ at the resonator port 4 (Fig. S3a). Fitting the spectral line-shape using master equation simulations we extract the Purcell decay rate γ_{Pur} which is a function of the tunable $|q_3\rangle$ frequency near the resonator fundamental mode $\omega_r/2\pi = 6.00$ GHz (Fig. S3b). The extracted values γ_{Pur} for positive detunings above the resonator frequency agree with Eq. (C1) with coupling $g/2\pi = 90$ MHz and resonator decay rate $\kappa/2\pi = 110$ MHz. For $\omega_3/2\pi = 6.198$ GHz used in the presented experiments (indicated

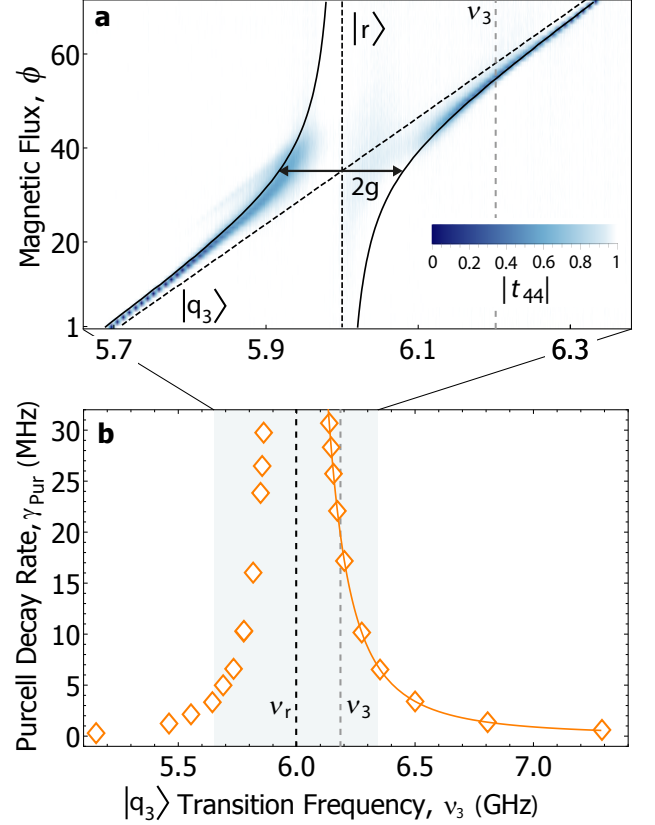


Figure S3: **Purcell decay of Q₃.** (a) Frequency dependent reflection coefficient $|t_{44}|$ as a function of magnetic flux where the $|q_3\rangle$ transition frequency ω_3 is swept linearly and the resonator fundamental frequency ω_r is fixed (displayed as black dashed lines). The gray dashed line corresponds to the $|q_3\rangle$ transition frequency $\omega_3/2\pi = 6.198$ GHz shown in Fig. 2b. (b) Q₃ Purcell decay rate γ_{Pur} as a function of Q₃ transition frequency extracted from the reflection coefficient measurements $|t_{44}|$. The resonator frequency $\omega_r/2\pi = 6.00$ GHz is indicated with a black dashed line. The solid line is a fit to Eq. (C1). The light blue area indicates the frequency range in (a) and the vertical gray dashed line indicates the $|q_3\rangle$ transition frequency, similar as in (a).

by the gray dashed line in Fig. S3b) the Purcell decay rate is $\gamma_{\text{Pur}}/2\pi \approx 20$ MHz.

Appendix D: Rabi Rate and PSD Calibration

The Rabi rate Ω_R of the coherently driven bright $|b\rangle$ state was determined from measurements of bright state resonance fluorescence power spectra $S_2(\omega)$ (Fig. S4). To obtain the Rabi rate $\Omega_R/2\pi = 14$ MHz for the microwave powers used in our experiments we fit the resonance fluorescence spectrum to the Mollow triplet expression⁹ assuming negligible pure dephasing and non-radiative decay. For larger applied microwave powers, the full Mollow triplet¹⁰ of the bright state emerges with resolved side

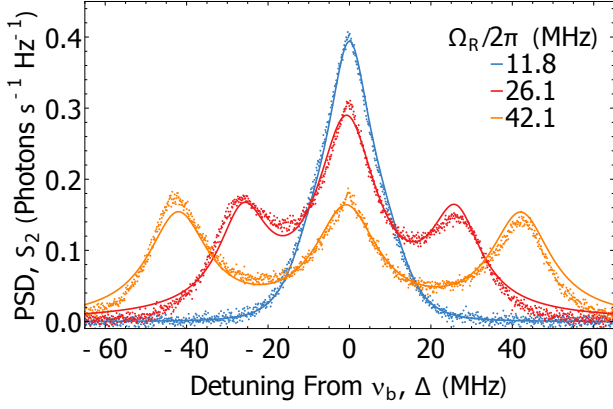


Figure S4: **Mollow triplet of the bright state.** Measured power spectral density (PSD) $S_2(\omega)$ of the bright state resonance fluorescence emission spectrum at the output of the waveguide for indicated coherent microwave amplitudes given in terms of the extracted Rabi rate Ω_R . The microwave drive frequency was set to the bright state transition frequency ω_b . Solid lines are fits to the Mollow triplet spectrum⁹ for $\Omega_R/2\pi = 11.8$ MHz and to the sum of three Lorentzian functions for $\Omega_R/2\pi = 26.1$ and 42.1 MHz.

peaks. We determine the Rabi rate Ω_R for these amplitudes from the frequency splitting between the central and the side peaks when fitting the spectra with three Lorentzian lines. Fits to the data are shown with solid lines in Fig. S4.

In order to calibrate the amplitude of the measured power spectral densities we performed the same power spectrum measurement on Q_2 with all other qubits detuned by more than 1.5 GHz. For strong coherent drive, when the qubit is saturated, and assuming that pure dephasing and non-radiative decay rates are negligible the integrated power of the measured Mollow triplet is equal to $\gamma_1/2$ photons per unit time. This allows us to express the magnitude of measured PSD in $\text{Photons s}^{-1} \text{Hz}^{-1}$.

Appendix E: Noise Generation

Low frequency noise is generated from a filtered random number time series consisting of $16 \cdot 10^6$ values. The bandwidth of the generated noise spans from 75 Hz to 600 MHz. The time series with a desired power spectral density $S(\omega)$ is constructed by first calculating the Gaussian random number sequence with a unit power spectral density $S(\omega) = 1$ and then applying a finite impulse response filter (FIR) with the frequency response function $H(\omega)$. We compensate AWG signal discretization distortions by pre-equalizing the digital noise series with an additional filter, constructed from the AWG output spectrum of an ideal white noise digital signal measured using a spectrum analyzer.

In this work we consider two distinct power spectral

densities: (i) white noise with an exponential cutoff based on the Fermi-Dirac distribution

$$S_W(\omega) = \frac{A_W}{1 + e^{\frac{\omega - \omega_c}{\Delta\omega}}}, \quad (\text{E1})$$

where A_W is the amplitude of the function constant up to an exponential cutoff at $\omega_c/2\pi = 325$ MHz with a characteristic width $\Delta\omega/2\pi = 5.44$ MHz. (ii) Noise with a Lorentzian power spectral density:

$$S_L(\omega) = \frac{A_L}{1 + \left(\frac{\omega - \omega_L}{\Delta\omega_L/2}\right)^2}, \quad (\text{E2})$$

where A_L is the amplitude, $\omega_L/2\pi = 0 - 300$ MHz is the variable center frequency and $\Delta\omega_L/2\pi = 10$ MHz is the full width at half maximum. The noise power spectral densities in Fig. 2c in the main text are measured with a spectrum analyzer at the output of the AWG.

Appendix F: Pure Dephasing Rate Calibration

White noise applied to Q_2 increases the pure dephasing rate of $|q_2\rangle$ and consequently that of bright $|b\rangle$ and dark $|d\rangle$ states. The bright state pure dephasing rate γ_ϕ^b is determined from the resonance fluorescence power spectrum of the bright mode measured through the waveguide $S_2(\omega)$ for indicated applied noise powers Φ_W^2 (see Fig. S5a). Measured spectra are fitted to the Mollow triplet expression⁹ with the pure dephasing rate γ_ϕ^b as a free parameter and fixed center frequency ω_0 , Rabi rate Ω_R and decay rate γ_b . The extracted pure dephasing rate γ_ϕ^b (see Fig. S5b) shows an initial linear increase with applied white noise power Φ_W^2 as expected for ideal Markovian white power spectral density PSD¹¹. Deviations from the linear dependence at higher noise powers originate from the finite cutoff of the engineered white noise (see Fig. 2c in the main text). The numerically calculated pure dephasing rate¹¹ using a noise power spectral density with a finite cutoff is in excellent agreement with the data (solid line in Fig. S5b) indicating that the origin of the deviation from the linear dependence is the finite bandwidth of the engineered white noise.

Appendix G: White Noise PSD Analysis

We analyze power spectral densities $S_4(\omega)$ measured at the resonator as a function of applied environmental white noise power (see Fig. 3a and Fig. S6a) by fitting the spectra with a sum of two Lorentzian functions

$$F(\nu) = \frac{a_1}{1 + 4\left(\frac{\nu - \nu_{01}}{\Delta\nu_1}\right)^2} + \frac{a_2}{1 + 4\left(\frac{\nu - \nu_{20}}{\Delta\nu_2}\right)^2}. \quad (\text{G1})$$

Here a_i is the amplitude, ν_{0i} the center frequency and $\Delta\nu_i$ the full width at half maximum of the i -th Lorentzian.

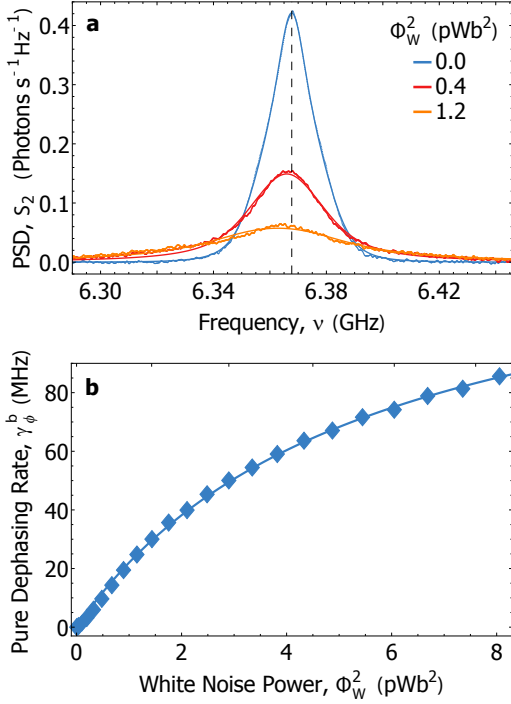


Figure S5: **Bright state dephasing rate.** (a) Measured power spectral density $S_2(\omega)$ of the bright mode at port 2 of the waveguide for indicated environmental applied white noise powers Φ_W^2 . Solid lines are fits to the Mollow-triplet spectrum⁹, see text. (b) Pure dephasing rate γ_ϕ^b of the bright mode as a function of white noise power Φ_W^2 obtained from the fitted bright state resonance fluorescence spectra. The solid curve is a numerical calculation of the pure dephasing rate γ_ϕ^b for the white noise power spectral density with a finite frequency cutoff at 325 MHz (see Fig. 2c in the main text).

For higher noise powers, for which the two peaks are not resolved anymore, we fit the data to a single Lorentzian. The two resonances centered near the spectroscopically determined transition frequencies ν_{d1} and ν_{d2} for low white noise powers gradually shift towards the bare $|q_3\rangle$ transition frequency ν_3 (Fig. S6b). At the same time the linewidth of the lower frequency resonance corresponding to $|d_1\rangle$ significantly broadens while the one corresponding to $|d_2\rangle$ remains unchanged (see Fig. S6c). The different dependence of the $|d_1\rangle$ and $|d_2\rangle$ resonances on the applied noise is attributed to an imperfect hybridization of the $|d\rangle$ and $|q_3\rangle$ states. From the analyzed data we determine the cross-over from the strong to the weak coupling regime to occur at $\Phi_W^2 = 3.0 \pm 1.0 \text{ pWb}^2$ corresponding to $\gamma_\phi^b/2\pi = 50 \pm 10 \text{ MHz}$. This value is comparable to the $2J_{d3}/2\pi = 37 \text{ MHz}$, which is in agreement with the crossover from strong to weak coupling as discussed in the main text.

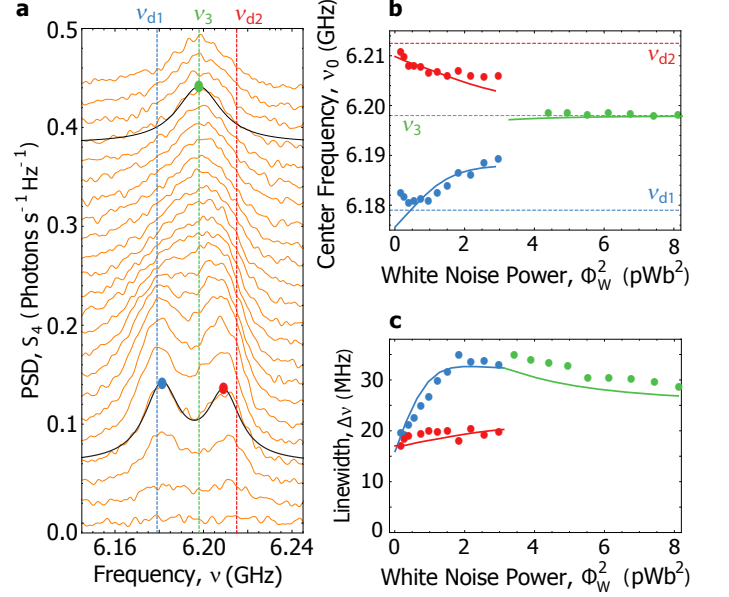


Figure S6: **Spectra of $|d_1\rangle$ and $|d_2\rangle$ dark states.** (a) Power spectral density $S_4(\omega)$ at the resonator output port 4 for applied environmental white noise powers Φ_W^2 ranging from 0 to 8.1 pWb^2 . Black solid curves show two selected fits to the data using two Lorentzian functions ($\Phi_W^2 = 0.6 \text{ pWb}^2$) and a single Lorentzian function ($\Phi_W^2 = 6.1 \text{ pWb}^2$). Vertical dashed lines indicate spectroscopically determined transition frequencies of $|d_1\rangle$ ($\nu_{d1} = 6.179 \text{ GHz}$), $|d_2\rangle$ ($\nu_{d2} = 6.216 \text{ GHz}$) and $|q_3\rangle$ ($\nu_3 = 6.198 \text{ GHz}$) states. (b) Lorentzian center frequencies as a function of white noise power Φ_W^2 from the fits (red, blue and green dots). Horizontal dashed lines mark $|d_1\rangle$, $|d_2\rangle$ and $|q_3\rangle$ transition frequencies as in (a). (c) Lorentzian full width at half maximum (fwhm) as a function of white noise power Φ_W^2 determined from fitting the power spectral densities indicated in (a). Solid lines in (b) and (c) are results from master equation simulations.

Appendix H: Theoretical Description

1. Master Equation

The unitary dynamics of the three coupled qubits where Q_3 is coupled to the extraction resonator and Q_1 and Q_2 are driven by a coherent tone applied to the waveguide is described by the Hamiltonian in the rotating wave approximation

$$\begin{aligned} \hat{\mathcal{H}}/\hbar = & \sum_{j=1}^3 \left[\frac{(\omega_j - \omega_{\text{in}})}{2} \hat{\sigma}_j^z + \sum_{k < j} J_{kj} (\hat{\sigma}_k^+ \hat{\sigma}_j^- + \hat{\sigma}_j^+ \hat{\sigma}_k^-) \right] \\ & + (\omega_r - \omega_{\text{in}}) \hat{a}^\dagger \hat{a} + g_3 (\hat{a}^\dagger \hat{\sigma}_3^- + \hat{\sigma}_3^+ \hat{a}) \\ & + \frac{\Omega_{R1}}{2} (\hat{\sigma}_1^+ + \hat{\sigma}_1^-) + \frac{\Omega_{R2}}{2} (\hat{\sigma}_2^+ + \hat{\sigma}_2^-), \end{aligned} \quad (\text{H1})$$

where $\hat{\sigma}_j^z$, $\hat{\sigma}_j^+ = (\hat{\sigma}_j^x + i\hat{\sigma}_j^y)/2$ and $\hat{\sigma}_j^- = (\hat{\sigma}_j^x - i\hat{\sigma}_j^y)/2$ are Pauli operators, \hat{a} (\hat{a}^\dagger) is the annihilation (creation)

operator of the resonator's harmonic mode, ω_{in} is the input microwave frequency and also the frequency of the reference frame. The applied low frequency noise to Q_2 is modeled as a time dependence of $\omega_2 \equiv \omega_2(t)$ (see App. I). Ω_{Rj} is the Rabi frequency for j -th qubit. In the case of ideal hybridization between Q_1 and Q_2 ($\omega_1 = \omega_2$) the Hamiltonian can be written in the bright and dark state bases as

$$\begin{aligned} \hat{\mathcal{H}}/\hbar = & \sum_{j=b,d,3} (\omega_j - \omega_{\text{in}}) \hat{\sigma}_j^+ \hat{\sigma}_j^- + (\omega_r - \omega_{\text{in}}) \hat{a}^\dagger \hat{a} \\ & + J_{b3} (\hat{\sigma}_b^+ \hat{\sigma}_3^- + \hat{\sigma}_3^+ \hat{\sigma}_b^-) - J_{d3} (\hat{\sigma}_d^+ \hat{\sigma}_3^- + \hat{\sigma}_3^+ \hat{\sigma}_d^-) \\ & + g (\hat{a}^\dagger \hat{\sigma}_3^- + \hat{\sigma}_3^+ \hat{a}) + \frac{\Omega_R}{2} (\hat{\sigma}_b^+ + \hat{\sigma}_b^-), \end{aligned} \quad (\text{H2})$$

where $\hat{\sigma}_b^\pm = (\hat{\sigma}_1^\pm + \hat{\sigma}_2^\pm)/\sqrt{2}$ and $\hat{\sigma}_d^\pm = (\hat{\sigma}_1^\pm - \hat{\sigma}_2^\pm)/\sqrt{2}$ are bright and dark state creation and annihilation operators, $\omega_b = \omega_1 + J_{12}$, $\omega_d = \omega_1 - J_{12}$ are bright and dark state transition frequencies, $J_{b3} = (J_{23} + J_{13})/\sqrt{2}$ and $J_{d3} = (J_{23} - J_{13})/\sqrt{2}$ are coupling rates between Q_3 and bright, and Q_3 and dark state, respectively, and $\Omega_R = \sqrt{2}\Omega_{R1}$ is the bright state Rabi frequency.

The full dynamics including the non-unitary terms is given by the Lindblad equation

$$\dot{\rho} = \mathcal{L}(\rho), \quad (\text{H3})$$

where ρ is the density matrix and $\mathcal{L}(\rho)$ is given by

$$\begin{aligned} \mathcal{L}(\rho) = & -\frac{i}{\hbar} [\hat{\mathcal{H}}, \rho] \\ & + \gamma_b (1 + n_{\text{th}}) L(\sigma_b^-) \rho + \gamma_b n_{\text{th}} L(\sigma_b^+) \rho \\ & + \gamma_d (1 + n_{\text{th}}) L(\sigma_d^-) \rho + \gamma_d n_{\text{th}} L(\sigma_d^+) \rho \\ & + \frac{\gamma_\phi}{2} L(\sigma_2^+ \sigma_2^- - \sigma_2^- \sigma_2^+) \rho \\ & + \kappa L(a) \rho. \end{aligned} \quad (\text{H4})$$

Here $L(\sigma)$ is the Lindblad superoperator

$$L(\sigma)\rho = \hat{\sigma}\rho\hat{\sigma}^\dagger - \frac{1}{2}(\hat{\sigma}^\dagger\hat{\sigma}\rho + \rho\hat{\sigma}^\dagger\hat{\sigma}) \quad (\text{H5})$$

and $n_{\text{th}} < 0.01$, a typical thermal occupation for our experiments.

2. Simulations

Simulations of power spectral densities $S_2(\omega)$ at the waveguide output port 2 and the resonator $S_4(\omega)$ at port 4 as well as the integrated power at the waveguide P_2 , the resonator P_4 and the transfer efficiency η are performed with QuTiP 3.1.0¹². All simulations are done using the Lindblad master equation, which is sufficient for time independent decay channels, as well as the Bloch-Redfield master equation to account for the finite noise frequency cutoff (see Fig. 2c). Both methods yield identical results confirming that the noise PSD cutoff frequency

(≈ 325 MHz) is high enough for the interaction between our circuit and the environment to be considered in the Markovian approximation.

Waveguide and resonator spectra are calculated for the steady state $\dot{\rho} = 0$ via two-time correlation functions

$$s(\omega) = \int_{-\infty}^{\infty} \langle A(\tau) B(0) \rangle e^{-i\omega\tau} d\tau. \quad (\text{H6})$$

As a proxy for the waveguide emission we use the bright state $|b\rangle$ correlation function $\langle \hat{\sigma}_b^+(\tau) \hat{\sigma}_b^-(0) \rangle$ and for the resonator emission we use $\langle \hat{a}^\dagger(\tau) \hat{a}(0) \rangle$. The correct magnitude is achieved by multiplication with the respective radiative decay rates $\gamma_b/2$ and κ , where the factor 1/2 for the γ_b reflects the detection of only half of the photons emitted into the waveguide when measured only at port 2 and omitting port 1

$$\begin{aligned} S_2(\omega) & \approx \frac{\gamma_b}{2} \int_{-\infty}^{\infty} \langle \hat{\sigma}_b^+(\tau) \hat{\sigma}_b^-(0) \rangle e^{-i\omega\tau} d\tau, \\ S_4(\omega) & = \kappa \int_{-\infty}^{\infty} \langle \hat{a}^\dagger(\tau) \hat{a}(0) \rangle e^{-i\omega\tau} d\tau. \end{aligned} \quad (\text{H7})$$

As in the experimental analysis we obtain the full power as an integral of the power spectral density over frequency.

For the simulations shown in Fig. 3b and Figs. 4a,c, in the main text we use system parameters specified in Table I. In Figs. 4a,c of the main text the data is plotted against the bright state pure dephasing rate, which is related to the Q_2 pure dephasing rate as $\gamma_\phi^b = \gamma_\phi/2$ assuming that the bright state is an equal superposition of $|q_1\rangle$ and $|q_2\rangle$.

To reproduce experimental results for incoherent excitation a Lindblad master equation was solved without the last two terms in Eq. (H1). A thermal occupation of $n_{\text{th}} = 0.3$ was used to compute the integrated re-emitted P_2 and extracted P_4 powers as well as the transport efficiency η shown with solid lines in Fig. 4c.

3. Rate Equations

The rate equations for the populations of the bright $|b\rangle$ state $p_b = \rho_{bb}$, dark $|d\rangle$ state $p_d = \rho_{dd}$ and $|q_3\rangle$ state $p_3 = \rho_{33}$ are derived from the Lindblad equation of motion [Eq. (H3)] where the coupling of Q_3 to the resonator is approximated by an effective Purcell decay. The incoherent dephasing $\gamma_\phi/2 L[\sigma_2^z]\rho$, with $\gamma_\phi = 2\gamma_\phi^b$ leads to a decay of all coherences involving Q_2

$$\dot{\rho}_{i2} = -\gamma_\phi \rho_{i2} \quad \forall i \neq 2.$$

In the bright/dark state basis this operator describes incoherent transport $\gamma_\phi^b (L[\sigma_b^+ \sigma_d^-] + L[\sigma_d^+ \sigma_b^-])\rho$ between $|d\rangle$ and $|b\rangle$ towards an equilibrium population determined by

$$\frac{d}{dt}(\rho_{bb} - \rho_{dd}) = -2 \underbrace{\gamma_\phi^b}_{k_{bd}} (\rho_{bb} - \rho_{dd}),$$

Description	Parameter	Value
$ q_1\rangle$ transition frequency	$\omega_1/2\pi$	6.277 GHz
$ q_2\rangle$ transition frequency	$\omega_2/2\pi$	6.277 GHz
$ q_3\rangle$ transition frequency	$\omega_3/2\pi$	6.161 GHz
Resonator frequency	$\omega_r/2\pi$	6.000 GHz
Coupling between Q_1 and Q_2	$J_{12}/2\pi$	83.5 MHz
Coupling between Q_2 and Q_3	$J_{23}/2\pi$	33.4 MHz
Coupling between Q_1 and Q_3	$J_{13}/2\pi$	3.67 MHz
Coupling between Q_3 and the resonator	$g_3/2\pi$	90 MHz
$ b\rangle$ state decay rate	$\gamma_b/2\pi$	12.4 MHz
Resonator decay rate	$\kappa/2\pi$	110 MHz
Bright state Rabi rate	$\Omega_R/2\pi$	14.0 MHz
Input field frequency	$\omega_{in}/2\pi$	6.368 GHz

Table I: System parameters used for simulations. All parameters are experimentally determined from spectroscopic measurements except g and κ which were adjusted within their experimental uncertainty.

The bright state population $\dot{\rho}_{bb} \propto \Omega_R \text{Im}(\rho_{gb})$ is reduced by incoherent dephasing since the coherence between the ground and the bright state ρ_{gb} evolves as

$$\dot{\rho}_{gb} \propto i \frac{\Omega_R}{2} (\rho_{gg} - \rho_{bb}) - \frac{\gamma_b + 2\gamma_\phi^b}{2} \rho_{gb}.$$

Thus absorption is reduced by dephasing when $\gamma_\phi^b \gtrsim \Omega_R$. In the steady state the bright state population can be written as

$$\dot{\rho}_{bb} \propto \frac{\Omega_R^2}{\gamma_b + 2\gamma_\phi^b} (\rho_{gg} - \rho_{bb}).$$

The coherent population transfer from $|d\rangle$ to $|q_3\rangle$ is defined by their coherence

$$\frac{d}{dt}(\rho_{dd} - \rho_{33}) \propto -4J_{d3} \text{Im}(\rho_{d3}),$$

which in turn is controlled by the coherent coupling and the incoherent dephasing

$$\dot{\rho}_{d3} \propto -iJ_{d3}(\rho_{33} - \rho_{dd} + \rho_{db}) - \frac{\gamma_{\text{Pur}} + 2\gamma_\phi^b}{2} \rho_{d3}.$$

The scale at which coherent transport is expected to be reduced due to noise is $\gamma_\phi^b \gtrsim J_{d3}$. To derive the Förster transport rates k_{gb} between the ground $|g\rangle$ and the bright state $|b\rangle$ and the dark $|d\rangle$ and $|q_3\rangle$ state k_{d3} in the strong dephasing limit we assume that coherences are small, if they are not participating in transport, and that derivatives of coherences are negligible¹³. For $\rho_{db} \approx 0$ and $\dot{\rho}_{d3} = \dot{\rho}_{gb} = 0$ we therefore have

$$\begin{aligned} \rho_{d3} &= i \frac{-J_{d3}}{\gamma_{\text{Pur}}/2 + \gamma_\phi^b} (\rho_{33} - \rho_{dd}), \\ \rho_{gb} &= i \frac{\Omega_R}{\gamma_b + 2\gamma_\phi^b} (\rho_{gg} - \rho_{bb}). \end{aligned} \quad (\text{H8})$$

With the help of the above expressions we find the rate equations

$$\begin{aligned} \dot{p}_g &= -k_{gb}(p_g - p_b) + \gamma_b p_b + \gamma_{\text{Pur}} p_3, \\ \dot{p}_b &= k_{gb}(p_g - p_b) - k_{bd}(p_b - p_d) - \gamma_b p_b, \\ \dot{p}_d &= k_{bd}(p_b - p_d) - k_{d3}(p_d - p_3), \\ \dot{p}_3 &= k_{d3}(p_d - p_3) - \gamma_{\text{Pur}} p_3, \end{aligned} \quad (\text{H9})$$

for $|g\rangle, |b\rangle, |d\rangle$ and $|q_3\rangle$ populations with transfer rates

$$\begin{aligned} k_{gb} &= \frac{\Omega_R^2}{\gamma_b + 2\gamma_\phi^b}, \\ k_{d3} &= \frac{4J_{d3}^2}{\gamma_{\text{Pur}} + 2\gamma_\phi^b}, \\ k_{bd} &= \gamma_\phi^b, \end{aligned}$$

where state populations are bound by $p_i \in [0, 1]$. Since $\gamma_b \approx \gamma_{\text{Pur}}$ and $\Omega_R \ll 2J_{d3}$, the reduction of absorption for increasing γ_ϕ^b happens before the complete decoupling of $|d\rangle$ and $|q_3\rangle$. From Eq. (H8) we see that population transfer between $|d\rangle$ and $|q_3\rangle$ is always coherent although $|d\rangle$ is populated incoherently and the transfer is suppressed by the dephasing rate γ_ϕ^b .

The transfer efficiency is calculated using steady state solutions of Eqs. (H9) as

$$\eta = \frac{\gamma_{\text{Pur}} p_3}{\gamma_{\text{Pur}} p_3 + \gamma_b p_b}, \quad (\text{H10})$$

where we assumed $p_g = 1$. The efficiency has a maximum at $\gamma_\phi^b = \sqrt{2}J_{d3} \approx J_{23}$ where it can be expressed as

$$\eta = \frac{1}{1 + \sqrt{2} \frac{\gamma_b}{J_{d3}} + \frac{\gamma_b}{\gamma_{\text{Pur}}} + \frac{\gamma_b \gamma_{\text{Pur}}}{4J_{d3}^2}}. \quad (\text{H11})$$

Assuming that $2J_{d3} \gg \gamma_b, \gamma_{\text{Pur}}$, the efficiency can be written as

$$\eta \approx (1 - \gamma_b/\gamma_{\text{Pur}}), \quad (\text{H12})$$

as stated in the main text.

4. Dephasing Rate due to Lorentzian Noise

Flux noise acting on Q_2 leads to an effective dephasing of the qubit with a dephasing rate depending on the noise power spectrum. In this section, we consider the effect of Lorentzian flux noise, in particular how it differs from white flux noise, and the emergence of non-Markovian effects. We study the essential physics with a single qubit model for Q_2 alone, described by the Hamiltonian

$$\mathcal{H}_2 = \frac{\omega_2}{2} \sigma_2^z + \xi(t) \sigma_2^z. \quad (\text{H13})$$

Here, ω_2 is the qubit transition frequency and $\xi(t)$ represents the input flux noise with power spectral density $S_{\xi\xi}[\omega]$,

$$\langle \xi(t) \rangle = 0, \quad S_{\xi\xi}[\omega] = \int_{-\infty}^{\infty} d\tau e^{-i\omega\tau} \langle \xi(\tau) \xi(0) \rangle \quad (\text{H14})$$

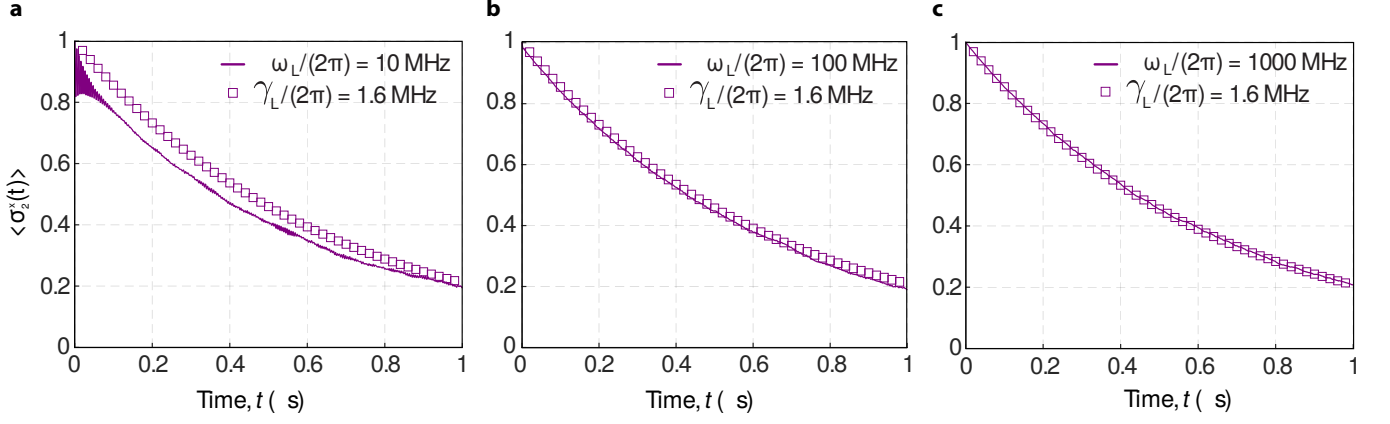


Figure S7: **Dephasing induced by Lorentzian noise.** Dynamics of $\langle \sigma_2^x(t) \rangle$ as a function of Lorentzian noise power bandwidth $\Delta\omega_L/2\pi = \{10, 100, 1000\}$ MHz. The noise amplitude A is decreased with increasing $\Delta\omega_L$ so as to keep γ_L fixed at $\gamma_L/2\pi = 1.6$ MHz. Open squares indicate a calculated exponential decay of $\langle \sigma_2^x(t) \rangle$ within the Markov approximation [see Eq. (H20)] for $\gamma_L/2\pi = 1.6$ MHz. As the Lorentzian noise correlation time $1/\Delta\omega_L$ decreases (left to right), the system dynamics are increasingly more faithfully described within the Markov approximation [Eq. (H20)].

In the experiment, $S_{\xi\xi}[\omega]$ is either a flat spectrum up to a certain cutoff frequency $S_W(\omega)$ [Eq. (E1)] or a Lorentzian spectrum $S_L[\omega]$ [Eq. (E2)].

The Hamiltonian [Eq. (H13)] is non-demolition with respect to σ_2^z since $[\mathcal{H}_2, \sigma_2^z] = 0$, but leads to an effective decay of $\langle \sigma_2^x \rangle$ and $\langle \sigma_2^y \rangle$ components, which we derive next. The effective dephasing rate is extracted by studying the dynamics of these observables. Moving into a frame rotating at ω_2 , we write the Heisenberg equations of motion for these operators as

$$\begin{aligned}\dot{\sigma}_2^x &= -2\xi(t)\sigma_2^y, \\ \dot{\sigma}_2^y &= +2\xi(t)\sigma_2^x.\end{aligned}\quad (\text{H15})$$

The above coupled system is formally solved to obtain a single dynamical equation for $\sigma_2^x(t)$. Averaging this equation under noise realizations, we arrive at

$$\dot{\sigma}_2^x(t) = -4 \int_0^t d\tau \langle \xi(t)\xi(t-\tau) \rangle \sigma_2^x(t-\tau). \quad (\text{H16})$$

Note that the noise autocorrelation appears in the above memory kernel; it is then possible to proceed via a Markovian approximation *provided* the noise correlations decay much faster than the relaxation dynamics of the system, which are themselves driven by the noise. We make this condition precise in a self-consistent way. Assuming Markovian approximation, we can drop the system's dependence on its past history via the memory kernel and extend the integral's upper limit to infinity, thus obtaining

$$\dot{\sigma}_2^x(t) = -4\sigma_2^x \int_0^\infty d\tau \langle \xi(\tau)\xi(0) \rangle. \quad (\text{H17})$$

The remaining integral is simply half the zero frequency power spectral density of the noise signal (ignoring the

principle part that leads to a Lamb shift contribution, not dephasing), so that

$$\dot{\sigma}_2^x(t) = -2S_{\xi\xi}[0] \cdot \sigma_2^x. \quad (\text{H18})$$

Hence, the noise signal drives system decay at a rate $2S_{\xi\xi}[0]$ *within* the Markovian approximation. For white noise, which is δ -correlated, correlations always decay faster than the induced decay. Using $S_{\xi\xi}[0]$ for white noise, the dephasing rate γ_ϕ is given by:

$$\gamma_\phi = 2A_W \quad (\text{H19})$$

More interesting is the case of Lorentzian noise. Eq. (H18) yields a decay rate γ_L for this case as well, so long as the Lorentzian noise ‘appears’ white, namely when the correlation time of the Lorentzian noise signal is much shorter than the time scale of the decay it induces, $1/\gamma_L$. Since the Lorentzian noise correlation time is on the order of its inverse bandwidth $1/\Delta\omega_L$, we require $1/\Delta\omega_L \ll 1/\gamma_L$, or $\Delta\omega_L \gg \gamma_L$. If this is the case, the dephasing rate is given by

$$\gamma_L = 2A_L \frac{\left(\frac{\Delta\omega_L}{2}\right)^2}{\omega_L^2 + \left(\frac{\Delta\omega_L}{2}\right)^2}, \quad \Delta\omega_L \gg \gamma_L. \quad (\text{H20})$$

Clearly, the dephasing rate is reduced compared to the white noise value for the same noise amplitudes ($A_W = A_L$). This is due to the colored noise spectrum which is not in fact equal at all frequencies.

However, we caution that the above expression holds only when the Lorentzian noise bandwidth is much larger than the induced decay rate, $\Delta\omega_L \gg \gamma_L$. In the current experiment, this condition is not met and the Markovian approximation should not hold. To observe dynamics in this regime for the simple single qubit model, we numerically compute the noise-averaged dynamics of

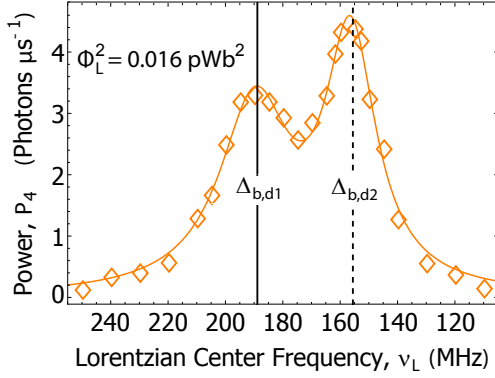


Figure S8: **Extracted power P_4 as a function of center frequency ν_L of Lorentzian noise spectrum.** This measurement was performed at Lorentzian noise power $\Phi_L^2 = 0.016$ pWb² and coherent excitation. Orange solid line is a fit to a sum of two Lorentzians.

$\langle \sigma_2^x \rangle$ as governed by \mathcal{H}_2 , over multiple realizations of the noise $\xi(t)$. By varying the bandwidth $\Delta\omega_L$ of the Lorentzian noise, we are able to explore both Markovian and non-Markovian regimes. For each $\Delta\omega_L$, the noise amplitude A is chosen such that the decay rate within the Markovian approximation has the fixed value $\gamma_L/2\pi = 1.6$ MHz. The dynamics of $\langle \sigma_2^x(t) \rangle$ (solid line in Fig. S7) for $\Delta\omega_L/2\pi = \{10, 100, 1000\}$ MHz increasing from left to right is approximately an exponential decay. As $\Delta\omega_L$ becomes large in comparison to γ_L - that is, when the noise correlation time $1/\Delta\omega_L$ becomes increasingly short relative to the noise-induced system relaxation time $1/\gamma_L$ - the Lorentzian noise-induced dynamics approach those predicted within the Markovian approximation (open squares in Fig. S7). Due to its non-Markovian effects Eq. (H18) does not exactly describe the decay of coherence for the Lorentzian noise, however, it offers a meaningful estimation that is used when comparing the effects of the two types of noise.

5. Simulations with Lorentzian Noise

Lorentzian noise spectra employed in the discussed experiments have bandwidths $\Delta\omega_L$ that are on the order of, or slower, than the pertinent circuit decay rates. This implies that noise autocorrelation decay times surpass typical system relaxation timescales. As such, a noise environment structured in this way can give rise to non-Markovian dynamics of the system density matrix: the system's state at time t can be affected by its history over a time set by the autocorrelation time of the applied noise. Note that this is the case even if the noise signal itself is entirely independent of the system evolution, as in the present setup, where the noise is algorithmically generated. Integrating out the Lorentzian noise signal yields complex memory kernels that cannot be collapsed, unlike the case for Markovian dynamics. Our approach

incorporates the Lorentzian noise environment as part of the system dynamics. In this way, we may still employ a Lindblad master equation for simulations of the system density matrix, at the cost of having to deal with a stochastic term describing the system's evolution.

To proceed, we add to the system Hamiltonian in Eq. (6) a modulation of the Q_2 energy splitting, given by the time series $\xi(t)$:

$$\mathcal{H}_\phi = \xi(t)\sigma_2^z \equiv \xi_0 \cos[\omega_L t + \phi(t)]\sigma_2^z \quad (\text{H21})$$

Here, $\phi(t)$ is a *random* variable describing phase noise, characterised by its statistical mean and variance:

$$\langle \phi \rangle = 0, \quad \langle \phi^2 \rangle = \Delta\omega_L t \quad (\text{H22})$$

The variance being linear in time indicates that the phase undergoes diffusion, with the parameter $\Delta\omega_L$ characterizing the strength of this diffusion. The phase noise $\phi(t)$ is often referred to as Brownian noise or a Wiener process in other contexts and is the integral of Gaussian white noise. $\xi(t)$ has a Lorentzian power spectral density¹⁴

$$S_{\xi\xi}(\omega) = \xi_0^2 \frac{\frac{\Delta\omega_L}{2}}{(\omega - \omega_L)^2 + \left(\frac{\Delta\omega_L}{2}\right)^2} \quad (\text{H23})$$

with a constant integrated power proportional to ξ_0^2 (independent of the value of $\Delta\omega_L$). Note that $S_{\xi\xi}(\omega)$ is written for $\omega > 0$; a symmetrical contribution exists for negative frequencies since $\xi(t)$ is a classical signal. Finally, note that taking $\Delta\omega_L \rightarrow 0$ formally yields a coherent modulation of the Q_2 energy splitting at frequency ω_L .

For small ξ_0 we solve the master equation, Eq. (H3), with the addition of \mathcal{H}_ϕ to the system Hamiltonian. The cost of adding a stochastic term to the system evolution is that any physical quantity must be computed via an explicit averaging procedure. In the Markovian approximation, an equivalent procedure is implicitly carried out when 'tracing out the bath'. For a given set of system parameters, we propagate the Master equation to long times to obtain an approximate steady state density matrix ρ_{ss} . Then, steady state correlation functions are computed starting with the system in ρ_{ss} . To obtain meaningful results, these computations are repeated over multiple realizations of $\xi(t)$; the relevant resonator and transmission line power spectra are then given respectively by:

$$S_2(\omega) = \quad (\text{H24})$$

$$\frac{\gamma_b}{2} \int_{-\infty}^{\infty} d\tau e^{-i\omega\tau} \langle (\sigma_b^+(\tau) - \langle \sigma_b^+ \rangle_{ss}) (\sigma_b^-(0) - \langle \sigma_b^- \rangle_{ss}) \rangle_\phi$$

$$S_4(\omega) = \kappa \int_{-\infty}^{\infty} d\tau e^{-i\omega\tau} \langle a^\dagger(\tau) a(0) \rangle_\phi \quad (\text{H25})$$

where $\langle \cdot \rangle_\phi$ indicates an ensemble average over multiple realizations of $\phi(t)$. The subtraction of steady state averages from the bright state correlation function serves

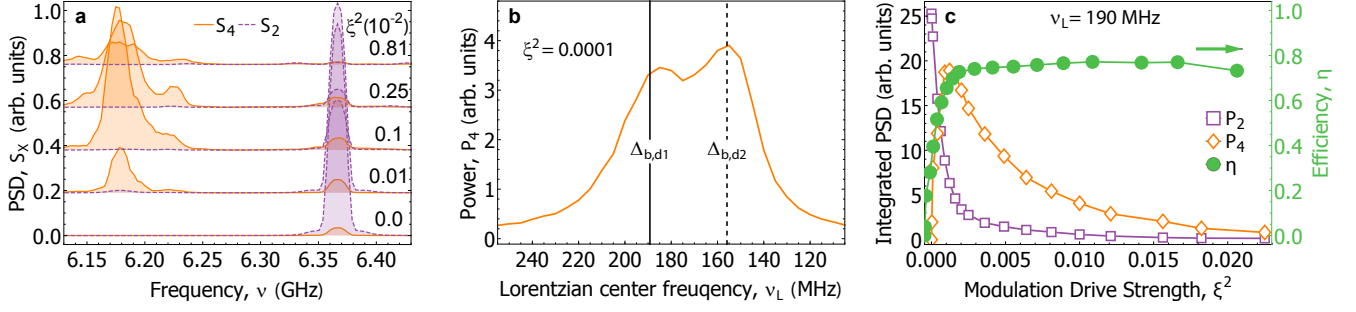


Figure S9: **Stochastically averaged master equation simulations.** (a) Power spectral density calculated at the resonator $S_4(\omega)$ (orange) and waveguide $S_2(\omega)$ (purple) output for Lorentzian noise with a center frequency of $\nu_c = 190$ MHz and variable modulation drive strength ξ^2 . (b) Calculated integrated power P_4 as a function of the Lorentzian center frequency ν_L at fixed modulation drive strength $\xi^2 = 0.0001$. (c) Integrated powers P_2 (purple) and P_4 (orange) and the transfer efficiency η (green) as a function of Lorentzian noise modulation drive strength ξ^2 . Power spectra at lowest noise power are matched with experiment to fix overall scaling factors, which are then used to scale all other spectra.

to remove the Rayleigh scattered peak from the transmission spectrum.

For stationary problems, a variety of methods exist to compute the above power spectra directly in the frequency domain, foregoing the need for a Fourier transform. Such techniques do not apply here, following inclusion of the explicitly time-dependent Lorentzian noise term. We find that the aperiodic, finite nature of computed correlation functions here leads to well known artifacts in their numerical Fourier transforms, namely a broad noise spectrum in the frequency domain due to spectral leakage. To suppress this noise, we apply a standard, total-power-preserving (Blackman) windowing function prior to performing the Fourier transform. This technique non-uniformly modifies the power at every frequency component, in different ways for each correlation function, restricting us to making only qualitative comparisons with experiment.

Simulated spectra $S_4(\omega)$ and $S_2(\omega)$ as a function of increasing Lorentzian noise power (Fig. S9a), integrated power at the resonator P_4 as a function of Lorentzian center frequency ν_L (Fig. S9b) and the integrated power at the resonator P_4 , the open waveguide P_2 and the transport efficiency η as a function of Lorentzian noise power (Fig. S9c) are all in good qualitative agreement with the experimental results (Figs. 3c, 4b and S8).

Appendix I: Effective Qubit-Environment coupling

Engineered noise with Lorentzian PSD emulates coupling of Q_2 to a classical phononic mode at center frequency ω_L and spectral width $\Delta\omega_L$. We can estimate the effective qubit-environment coupling by decomposing the applied flux into a large static and a small fluctuating component $[\Phi(t) = \Phi_0 + \Delta\Phi(t)]$. Using Eq. (A1) the qubit transition energy can be decomposed as

$$H_q/\hbar = \omega(t)\sigma_2^z = \omega_0\sigma_2^z + \sigma_2^z \left. \frac{d\omega}{d\Phi} \right|_{\Phi_0} \cdot \Delta\Phi(t). \quad (\text{I1})$$

By assuming that a phononic environmental mode carries at most a single excitation its harmonic spectrum can be effectively substituted by that of a two-level system

$$H_q/\hbar \approx \omega_0\sigma_2^z + K\sigma_2^z \left[\sigma_{\text{ph}}^x(t) + \sigma_{\text{ph}}^{x\dagger}(t) \right], \quad (\text{I2})$$

where $K = d\omega/d\Phi \cdot \Delta\Phi_0$ is an effective qubit-environment coupling constant and (σ_{ph}^x) is dimensionless Pauli operator with unit magnitude.

For experiments with Lorentzian noise we estimate the effective qubit-environment coupling constant (K) as a root-mean-square of Q_2 transition frequency fluctuation induced by applied structured noise.

Appendix J: Modulating the Transition Frequency of Q_2 with a Coherent Tone

In order to elucidate the mechanism of energy transport for Lorentzian noise applied to Q_2 we perform an additional measurement in which the Q_2 transition frequency is coherently modulated via the flux line while it is simultaneously coherently driven via the waveguide. This corresponds to the limiting case of very narrow noise power spectral density. We initially adjust the frequency of the coherent tone ν_c to be equal to the $|b\rangle$, $|d_1\rangle$ frequency difference $\Delta_{b,d1}$ as in the Lorentzian noise case.

Measurements of the power spectral density at the resonator $S_4(\omega)$ show, similarly to the Lorentzian noise case (see Fig. 3c), a pronounced resonance at $|d_1\rangle$ frequency composed of a broad part with linewidth of approx. 20 MHz and a strong narrow peak with the linewidth of approx. 500 kHz (see Fig. S10a). The narrow peak is comparable in width with the environmental bright $|b\rangle$ state pure dephasing rate $\gamma_\phi^b/2\pi = 380$ kHz which indicates that it probably originates from the broadened and frequency shifted coherent microwave drive tone applied to the waveguide. When sweeping ν_c between 100 and 250 MHz and keeping the power

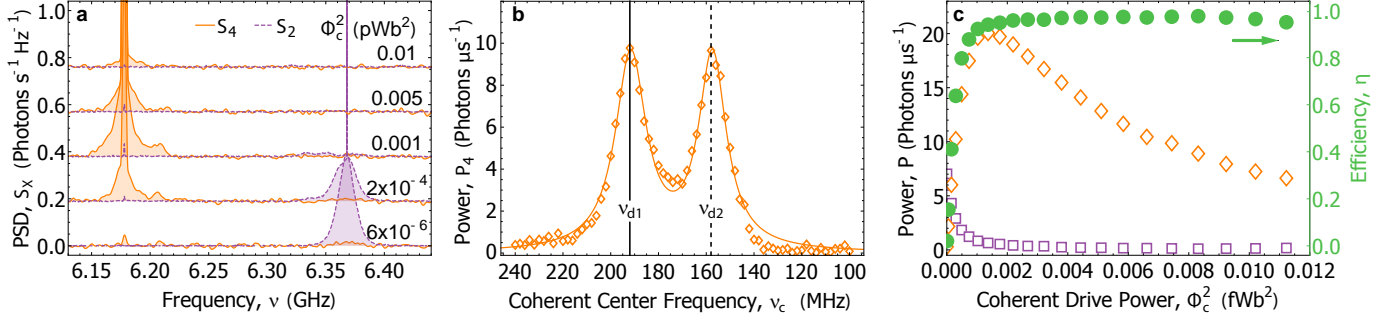


Figure S10: **Coherent environmental modulation of Q_2 transition frequency.** (a) Measured power spectral densities of radiation extracted from the resonator $S_4(\omega)$ (solid orange lines) and re-emitted into the transmission line $S_2(\omega)$ (dashed purple lines) for coherent modulation of Q_2 transition frequency with center frequency at $\nu_c = 190$ MHz and indicated powers Φ_c^2 . (b) Integrated extracted power P_4 as a function of coherent modulation frequency ν_c at fixed modulation tone power $\Phi_c^2 = 54.6$ aWb². (c) Integrated powers P_2 and P_4 and the transfer efficiency η as a function of coherent modulation power Φ_c^2 .

of the modulation tone constant at $\Phi_c^2 = 54.6$ aWb², P_4 shows similar dependence as in the white noise case where the extracted power is maximized for $\nu_c = \Delta_{b,d1}$ or $\Delta_{b,d1}$ (Fig. S10b). The linewidth of the resonances $\Delta\nu_{d1} = 14.1$ MHz and $\Delta\nu_{d2} = 15.7$ MHz correspond to the $|d_1\rangle$ and $|d_2\rangle$ state spectral widths. In the case of Lorentzian noise these were additionally broadened by the Lorentzian PSD width of $\Delta\nu_L = 10$ MHz, which resulted in $\Delta\nu_{d1,L} = 30.0$ MHz and $\Delta\nu_{d2,L} = 21.5$ MHz (see fit in Fig. S8).

For the low frequency coherent modulation the integrated power extracted from the resonator P_4 for $\nu_c = \Delta_{b,d1}$ is almost twice as large as in the Lorentzian noise case (see Fig. S10c and Fig. 4b), with approximately half of the power originating from the narrow peak at $|d_1\rangle$. The enhanced value of P_4 is in agreement with the model proposed in the main text. The integrated power of the radiation re-emitted into the waveguide P_2 is significantly smaller (0.7 Photons/ μ s) when P_4 reaches its maximum, as compared to white noise (Fig. 4a) or Lorentzian noise (Fig. 4b) case. As a result the internal transfer efficiency, as defined in the main text, reaches maximum values above 95%. Although not relevant for light-harvesting processes the depletion of the bright $|b\rangle$ state population is a result of coherent population trapping in the $|d_1\rangle$ state and electromagnetic induced transparency (EIT) of the bright $|b\rangle$ state. In our experiment EIT originates from the destructive interference between coherent excitation of the bright state $|b\rangle$ and strong coherent exchange between $|d_1\rangle$ and $|b\rangle$ state due to low frequency coherent modulation of Q_2 transition frequency^{15,16}.

Appendix K: Excitation with Incoherent Microwave Radiation

1. Engineering Incoherent Radiation

We engineer a broadband incoherent microwave signal by up-converting white noise (see App. E). In the

up-conversion process the high-frequency LO2 tone is multiplied by a low-frequency signal generated with an AWG (see inset to Fig. S11). In our experiment, low-frequency white noise with flat spectral density up to $\omega_c/2\pi = 450$ MHz and exponential cutoff with characteristic width $\Delta\omega/2\pi = 5.44$ MHz is up-converted using a coherent tone at $\omega_{LO2}/2\pi = 6.371$ GHz. The resulting high-frequency incoherent signal has a power spectral density with a constant amplitude that spans over a 900 MHz wide band centered at $\omega_B/2\pi = 6.371$ GHz as shown in Fig. S11. The attenuated incoherent signal is applied to the sample at port 1, similar to the RF line in Fig. S1.

2. Incoherently Excited System Subject to Lorentzian Noise

Applying Lorentzian noise to the incoherently excited system with central frequency $\nu_L = 190$ MHz set at the $|b\rangle$ - $|d_1\rangle$ frequency difference we observe no enhancement of the extracted power $S_4(\omega)$ at ν_{d1} relative to ν_{d2}

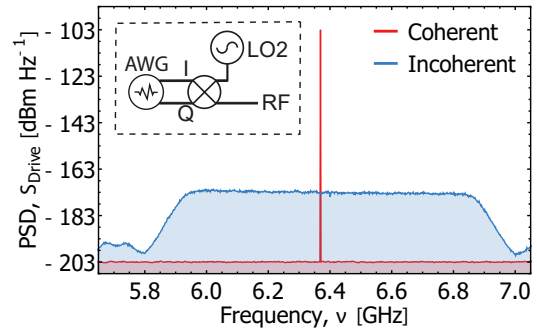


Figure S11: **Power spectral density of applied microwave signals.** Comparison between incoherent (blue) and coherent microwave signal (red), measured with a spectrum analyzer. The inset shows a diagram of the up-conversion process.

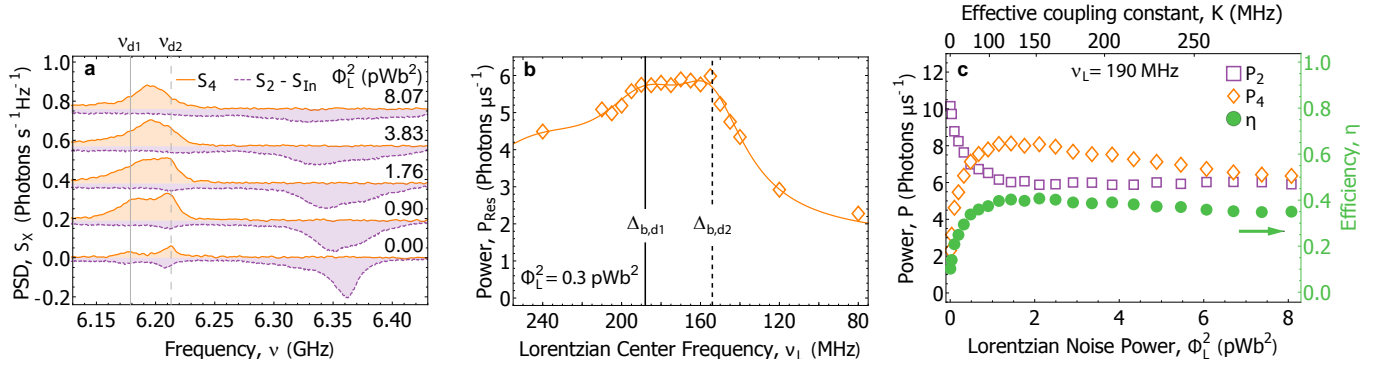


Figure S12: **Incoherently excited system subject to Lorentzian noise.** (a) Power spectral density detected at the resonator $S_4(\omega)$ (solid orange line) and at the waveguide $S_2(\omega)$ subtracted by separately measured incoherent radiation PSD (dashed purple line) as a function of Lorentzian noise power. (b) Integrated extracted power P_4 as a function of the center frequency ν_c of the Lorentzian noise at fixed noise power of $\Phi_L^2 = 0.3$ pWb². Solid orange line is a guide to the eye. (c) Integrated powers P_2 and P_4 and the transfer efficiency η as a function of Lorentzian noise power Φ_L^2 or equivalently the effective qubit-environment coupling constant K . The Lorentzian spectrum is centered at $\nu_c = 190$ MHz for (a) and (b).

(Fig. S12a) as in the case of coherent excitation. Contrary to the coherent excitation where a multi-photon process is fixed in frequency by a coherent tone, for the incoherent excitation a multi-photon process occurs over a larger frequency range and therefore does not produce a pronounced peak at the $|b\rangle$ - $|d_1\rangle$ frequency difference.

The Lorentzian noise increases the transferred power P_4 when resonant with the $|d\rangle$ and $|d_1\rangle$ or $|d_2\rangle$ frequency difference (Fig. S12b) similar to the coherent excitation case. The transfer efficiency η (Fig. S12c) shows a non-monotonic behaviour as a function of applied Lorentzian noise power Φ_L^2 or effective coupling constant K with the maximum at $K/2\pi \approx 130$ MHz, similar to the coherent excitation case. However, the maximal efficiency

$\eta_{L,inc.}^{\max} = 41\%$ is considerably lower compared to the coherent excitation and Lorentzian noise. The reduced efficiency can be attributed to the absence of a resonant multi-photon process, which increases the efficiency of the coherently excited system. On the other hand, the maximal efficiency obtained with Lorentzian noise ($\eta_{L,inc.}^{\max}$) is larger than the maximal efficiency obtained with white noise ($\eta_{W,inc.}^{\max}$). This is in agreement with observations for the coherently excited qubit system. We conclude that the narrow Lorentzian noise spectrum enhances the excitation transport when resonant with the appropriate energy level mismatch for both coherently and incoherently excited qubit systems.

* These authors contributed equally to this work

- ¹ Barends, R. *et al.* Coherent josephson qubit suitable for scalable quantum integrated circuits. *Phys. Rev. Lett.* **111**, 080502– (2013).
- ² Koch, J. *et al.* Charge-insensitive qubit design derived from the Cooper pair box. *Phys. Rev. A* **76**, 042319 (2007).
- ³ da Silva, M. P., Bozyigit, D., Wallraff, A. & Blais, A. Schemes for the observation of photon correlation functions in circuit QED with linear detectors. *Phys. Rev. A* **82**, 043804–12 (2010).
- ⁴ Fink, J. M. *et al.* Quantum-to-classical transition in cavity quantum electrodynamics. *Phys. Rev. Lett.* **105**, 163601 (2010).
- ⁵ Astafiev, O. *et al.* Resonance fluorescence of a single artificial atom. *Science* **327**, 840–843 (2010).
- ⁶ Purcell, E. M. Spontaneous emission probabilities at radio frequencies. *Phys. Rev.* **69**, 681 (1946).
- ⁷ Houck, A. A. *et al.* Controlling the spontaneous emission of a superconducting transmon qubit. *Phys. Rev. Lett.* **101**, 080502–4 (2008).
- ⁸ Sete, E. A., Gambetta, J. M. & Korotkov, A. N. Purcell effect with microwave drive: suppression of qubit relaxation

- rate. *Phys. Rev. B* **89**, 104516 (2014).
- ⁹ Carmichael, H. J. *Statistical Methods in Quantum Optics 1: Master Equations and Fokker-Planck Equations* (Springer, Berlin, 2002), 2 edn.
- ¹⁰ Mollow, B. R. Power spectrum of light scattered by two-level systems. *Phys. Rev.* **188**, 1969–1975 (1969).
- ¹¹ Martinis, J. M., Nam, S., Aumentado, J., Lang, K. & C., U. Decoherence of a superconducting qubit due to bias noise. *Phys. Rev. B* **67**, (9):094510 (2003).
- ¹² Johansson, J. R., Nation, P. D. & Nori, F. QuTiP 2: A Python framework for the dynamics of open quantum systems. *Comput. Phys. Commun.* **184**, 1234–1240 (2013).
- ¹³ Zhang, Y., Celardo, G. L., Borgonovi, F. & Kaplan, L. Opening-assisted coherent transport in the semiclassical regime. *Phys. Rev. E* **95**, 022122 (2017).
- ¹⁴ Lax, M. Classical Noise. V. Noise in Self-Sustained Oscillators. *Phys. Rev.* **160**, 290–307 (1967).
- ¹⁵ Abdumalikov, A. A. *et al.* Electromagnetically induced transparency on a single artificial atom. *Phys. Rev. Lett.* **104**, 193601 (2010).
- ¹⁶ Novikov, S. *et al.* Raman coherence in a circuit quantum electrodynamics lambda system. *Nature Phys.* **12**, 75

(2016).